Two-stage enrichment of germanium in the giant Maoping MVT Pb-Zn deposit, southwestern China: Constraints from in situ analysis of multicolor sphalerites

Pan-Pan Niu, Shao-Yong Jiang, Manuel Muñoz

Ore Geology Reviews 157 (2023) 105421

Contents lists available at ScienceDirect

Ore Geology Reviews

journal homepage: www.elsevier.com/locate/oregeorev

Two-stage enrichment of germanium in the giant Maoping MVT Pb-Zn deposit, southwestern China: Constraints from in situ analysis of multicolor sphalerites

Pan-Pan Niu [a,b,c], Shao-Yong Jiang [a,b,*], Manuel Muñoz [c]

[a] State Key Laboratory of Geological Processes and Mineral Resources, School of Earth Resources, Collaborative Innovation Center for Exploration of Strategic Mineral Resources, China University of Geosciences, Wuhan 430074, PR China
[b] Key Laboratory of Geological Survey and Evaluation of Ministry of Education, China University of Geosciences, Wuhan 430074, PR China
[c] Geosciences Montpellier, University of Montpellier, CNRS, Montpellier 34095, France

ARTICLE INFO

Keywords:
Germanium
Enrichment mechanism
Multicolor sphalerites
In situ analysis
Maoping deposit

ABSTRACT

The Maoping Pb-Zn deposit is one of the largest deposits in the Sichuan-Yunnan-Guizhou (SYG) MVT province in southwest China, which is also one of the biggest germanium producers in China. The hydrothermal mineralization process in this deposit can be divided into: (I) dolomite-pyrite stage, (II) sphalerite-galena stage, and (III) calcite stage. Five colors of sphalerites are recognized, including (C1) black, (C2) red brown, (C3) deep brown, (C4) light brown, and (C5) light red sphalerite. Pure colored C1, C2, C3 and C4 are dominanting in the entire sphalerite sequence, and there are also few rhythmic zonal sphalerites (e.g., Z1, Z2) composed of above four colored sphalerites. The C5 sphalerite precipitates last, and often cross-cuts other colored sphalerites in fine veins. Galena usually postdates than multicolor sphalerites. Based on μ-XRF and LA-ICP-MS mapping analysis, the Fe and Cu respectively dominate the variations of many other trace elements (e.g., Mn, Ag, Cd, Ga, Ge). The C5 and C1 sphalerites show the highest germanium contents (geometric mean 49 ppm for C5; 22 ppm for C1), followed by C4 (geometric mean 13 ppm). The contents of germanium and copper show a strong linear correlation for all colored sphalerites, in which germanium incorporates into sphalerite by the mechanism of $2Cu^{+} + Ge^{4+} \rightarrow 3Zn^{2+}$, while the nano-inclusion of Cu(Ag)-As(Ga)-S sulfosalt may evenly distribute in C5 sphalerite, resulting in its higher $(Cu/Ge)_{mol}$ ratios. According to the temperature and sulfur fugacity deduced from element compositions of sphalerite, the higher sulfur fugacity is more beneficial to the enrichment of germanium, relative to temperature. The sulfur isotope data suggest that the sulfur in C1, C2, C3 and C4 sphalerites originated from the Zaige and Baizuo Formations via bacterial sulfide reduction (BSR), in contrast to the sulfur in C5 sphalerite that mainly derived from the Datang Formation, with significantly higher sulfur fugacity and lower temperature. It is concluded that the fluids with germanium and reduced-sulfur derived from the Zaige and Baizuo Formations, mixed with the metal-bearing (e.g., Pb, Zn, Ag) basin brine, and caused the first-stage germanium enrichment in C1, C2, C3 and C4 sphalerites. Then the second-stage enrichment of germanium in C5 sphalerite was due to the involvement of fluid with germanium and reduced-sulfur derived from the Datang Formation.

1. Introduction

Sphalerite is the main ore mineral of Pb-Zn deposits in the world, which also hosts many economic critical metals, such as Cd, Ga, Ge, In, and Co (Cook et al., 2009; Ye et al., 2011; Bauer et al., 2019; Xu et al., 2021). Generally, these critical metals occur as solid solution in sphalerite, and rarely as independent minerals (e.g., Pfaff et al., 2011; Belissont et al., 2014; Cugerone et al., 2021; Mishra et al., 2021). The elemental contents and ratios (e.g., In, Cd, Ge, Co, In, Tl) are extensively used to determine the genetic type of the deposit, such as MVT, SEDEX, VMS, Skarn, CRD and epithermal-style (Liu et al., 2021; Hu et al., 2021; Xing et al., 2021; Mishra et al., 2021).

Globally, sphalerite is one of the important sources of germanium (Shanks et al., 2017). From the elemental content and linear correlation,

* Corresponding author at: State Key Laboratory of Geological Processes and Mineral Resources, School of Earth Resources, Collaborative Innovation Center for Exploration of Strategic Mineral Resources, China University of Geosciences, Wuhan 430074, PR China.
E-mail address: shyjiang@cug.edu.cn (S.-Y. Jiang).

https://doi.org/10.1016/j.oregeorev.2023.105421
Received 11 November 2022; Received in revised form 27 March 2023; Accepted 27 March 2023
Available online 28 March 2023

various Ge substitution mechanisms into sphalerite have been proposed, including (1) single: $Ge^{2+} \rightarrow 2Zn^{2+}$ (Pfaff et al., 2011; Yu et al., 2021), (2) binary: $2Fe^{2+} + Ge^{4+} \rightarrow 4Zn^{2+}$, $2Ag^{+} + Ge^{4+} \rightarrow 3Zn^{2+}$, $2Cu^{+} + Ge^{4+} \rightarrow 3Zn^{2+}$, $nCu^{2+} + Ge^{4+} \rightarrow (n+1)Zn^{2+}$, $Ge^{4+} + \square \rightarrow 2Zn^{2+}$, $Mn^{2+} + Ge^{2+} \rightarrow 3Zn^{2+}$, $Pb^{2+} + Ge^{2+} \rightarrow 2Zn^{2+}$ (Cook et al., 2009; Ye et al., 2019; Wu et al., 2019; Wei et al., 2019; Hu et al., 2021; Luo et al., 2022); (3) ternary: $2Cu^{+} + Fe^{2+} + Ge^{4+} \rightarrow 4Zn^{2+}$, $2Cu^{+} + Cu^{2+} + Ge^{4+} \rightarrow 4Zn^{2+}$, $2Fe^{2+} + Ge^{4+} + \square \rightarrow 4Zn^{2+}$, $Mn^{2+} + Ge^{4+} + \square \rightarrow 3Zn^{2+}$, $Pb(Mn)^{2+} + Ge^{4+} + \square \rightarrow 3Zn^{2+}$, $Cu(Ag)^{+} + Ga(As, Sb)^{3+} + Ge^{4+} \rightarrow 4Zn^{2+}$ (Bonnet et al., 2014; Cugerone et al., 2021; Yuan et al., 2018; Hu et al., 2021; Liu et al., 2022; Luo et al., 2022); (4) multivariate: $Ge^{4+} + 2(Cu + Ag + Tl)^{+} \rightarrow 3Zn^{2+}$, $4(Cu^{+} + Sb^{3+}) + (Ge^{4+} + 2Ag^{+}) + 2\square \rightarrow 13Zn^{2+}$ (Li et al., 2020; Torró et al., 2023). Some researchers have confirmed germanium in sphalerite in the form of tetravalent by X-ray absorption near edge structure (XANES) based on synchrotron (e.g., Cook et al., 2015; Belissont et al., 2016). In addition to entering the sphalerite structure, germanium can also form independent minerals in rare cases, for example, germanite, brunogeierite and stottite in the Arre (France), Tsumeb (Namibia) and Kipushi (Congo) deposits (Bernstein, 1985; Cugerone et al. 2019).

Germanium often exhibits the following properties in nature: (1) siderophile, (2) lithophile, (3) chalcophile, and (4) organophile (Bernstein, 1985; Höll et al., 2007). The MVT deposit, of which mineralization process is closely related to organic matter, is therefore an important deposit type for germanium (Leach et al., 2005; Han et al., 2007; Rosenberg, 2008). Hence, the black shale with high organic matter content is considered to be the important source of germanium in MVT Pb-Zn deposit, while the carbonate rocks with organic matter (e.g., bitumen) may also provide some germanium resources in the SYG area, SW China (Höll et al., 2007; Melcher and Buchholz, 2014; Han et al., 2015). The present study suggests that temperature plays a dominant role in the enrichment of germanium in sphalerite, and later dynamic metamorphism can cause germanium to precipitate from sphalerite to form tiny independent minerals (Cugerone et al., 2019; Liu et al., 2020).

The SYG area of China is a triangle district composed of the southwestern Sichuan Province, northeastern Yunnan Province and northwestern Guizhou Province (Xiang et al., 2020), where the Maoping Pb-Zn deposit is the second largest Pb-Zn deposit (20.3%, 12.51 Mt) and famous for its high grade Pb-Zn ores and huge germanium resources (Hu et al., 2017; Wu et al., 2021). The latest resource assessment report shows that the Maoping Pb-Zn deposit hosts more than 300 t Ge metal totally, and the present Ge retained reserve is 182 t (Chihong Mining

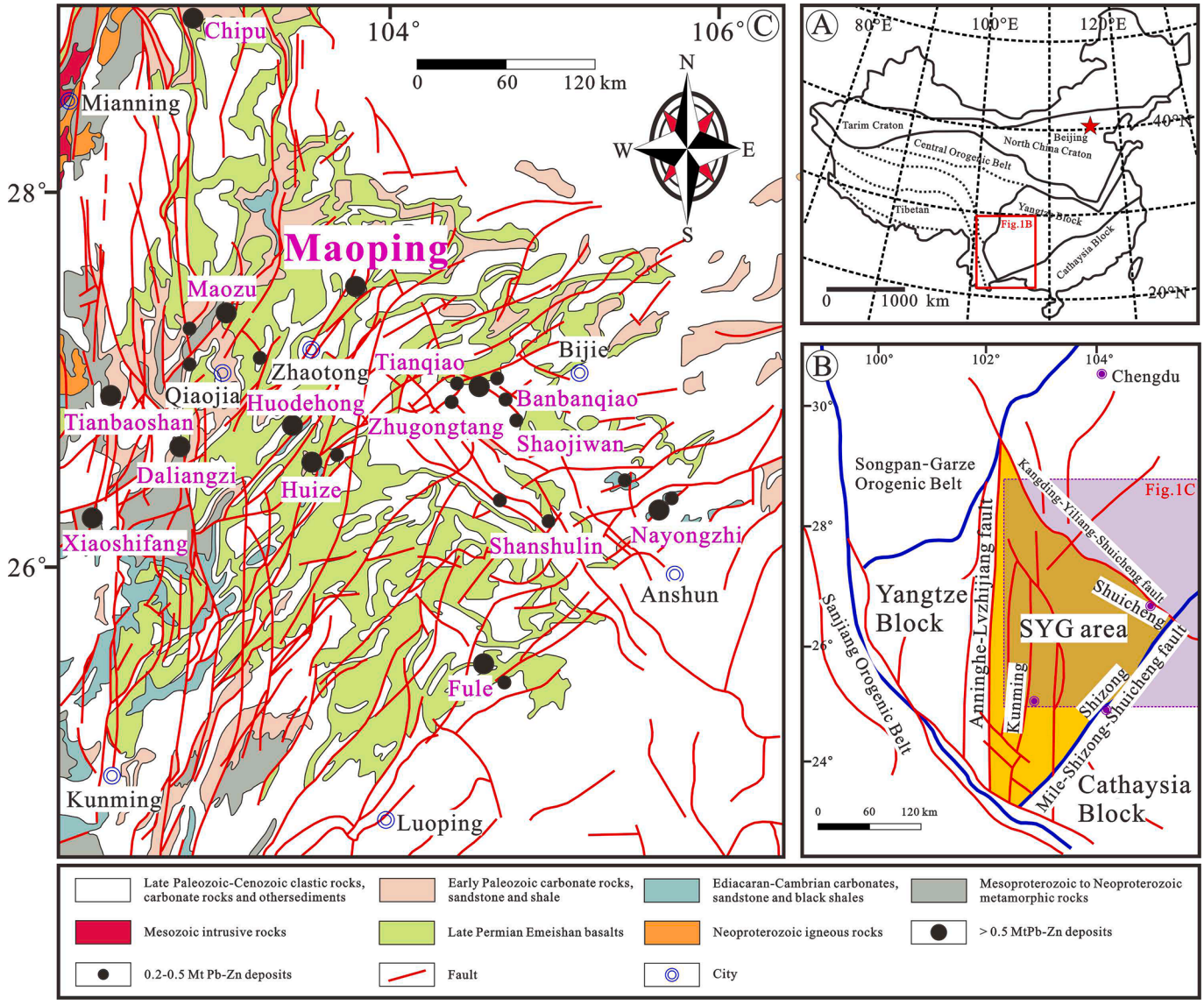

Fig. 1. (A) Tectonic framework of China (after Meng and Zhang, 2000), (B) Geological sketch map of southwest margin of the Yangtze Block in South China, also shown the triangular SYG area (after Ye et al., 2011), (C) Geological map of the SYG area showing strata, structure and Pb-Zn deposits (after Wei et al., 2021).

Co., LTD, 2018). Fluid mixing between metal-bearing basin brine and reduced sulfur fluids is widely considered as the key ore-forming mechanism of this deposit (e.g., Wu et al., 2021; Xiang et al., 2020). The present research on the Maoping deposit documents that Ge occurs as solid solution in sphalerite with concentration up to 652 ppm, but the exact elemental substitution of germanium into sphalerite is still unclear (e.g., Wei et al., 2021). In addition, the Ge enrichment mechanism and possible source in this deposit are still poorly understood due to limited research. In this study, based on detailed petrographic studies, we first identified multi-colored sphalerites that may derive from two different ore-forming fluids, and then carried out in-situ geochemical studies on multicolor sphalerites, including μ-XRF, EMPA, LA-ICP-MS and LA-MC-ICP-MS, in order to explore the Ge distribution and enrichment mechanism in sphalerite.

2. Geological background

The SYG area is located on the southwest margin of the Yangtze Block (Fig. 1A). Tectonically, the SYG area is restricted by the NW-trending Kangding-Yiliang-Shuicheng fault, the NS-trending Anninghe-Lvzhijiang fault and the NE-trending Mile-Shizong-Shuicheng fault, and a series of faults in this area also extend in the same direction as the above three faults (Fig. 1B; Xiang et al., 2020). The basement and double cover sequences (marine carbonates and continental sedimentary rocks), together with extensive Late Permian Emeishan basalts, constitute the geological units of the SYG area (Hu et al., 2017). The basement is the Neoproterozoic weakly metamorphosed strata (folded basement) widely distributed in the western of the SYG area, including the Kunyang/Huili and Yanbian Formations (Tan et al., 2019; Xiang et al., 2020). Neoproterozoic igneous rocks are mainly made up by mafic–ultramafic rocks and granitoids, which are only slightly distributed in the northwestern corner of the SYG area (Kong et al., 2018; Fig. 1C). From the late Neoproterozoic, the SYG area gradually evolved into a passive continental margin environment, and the thick marine carbonates were deposited in this area until the Triassic (Zhang et al., 2019). In the Late Permian of Paleozoic (~260 Ma), a huge mantle plume led to the formation of Emeishan basalts, which are widespread as a cap layer in the SYG area and cover > 250,000 km^2 in the southwestern Yangtze Block (Fig. 1C; He et al., 2020; Wei et al., 2021; Wu et al., 2021). Influenced by the Indosinian orogen, the SYG area was covered by abundant continental sedimentary rocks from the Jurassic to Quaternary (Yang et al., 2019). Miniature Mesozoic magmatism only formed small bodies of alkaline rock and granite in the northwestern of the SYG area (Liu and Lin, 1999).

The Maoping deposit is one of largest Pb-Zn deposit in the SYG area and hosts 12.51 Mt ores with average Pb + Zn grades of 20.3%, as well as existing 560 t Ag metals of 75 g/t grade and 182 t Ge metals with an average grade of 24 g/t. Bounded by the NW-trending Luoze river, the eastern I-III ore belt and the western Shuilu, Qiancengdong and Hongjianshan ore belts constitute principal part of the Maoping Pb-Zn deposit (Fig. 2A). The exposed strata in the Maoping deposit are composed of the Devonian Zaige Formation, the Carboniferous Datang, Baizuo and Weining Formations, the Permian Liangshan and Qixia-Maokou Formations, together with the Permian Emeishan basalts and Quaternary sediments. The lithologic and ore-bearing characteristics of the above strata are summarized in Fig. 3. The Shimenkan anticline, a plunging anticline with a short axis, is the main ore-controlling structure of the Maoping Pb-Zn deposit, and its axial direction spread out in the shape of

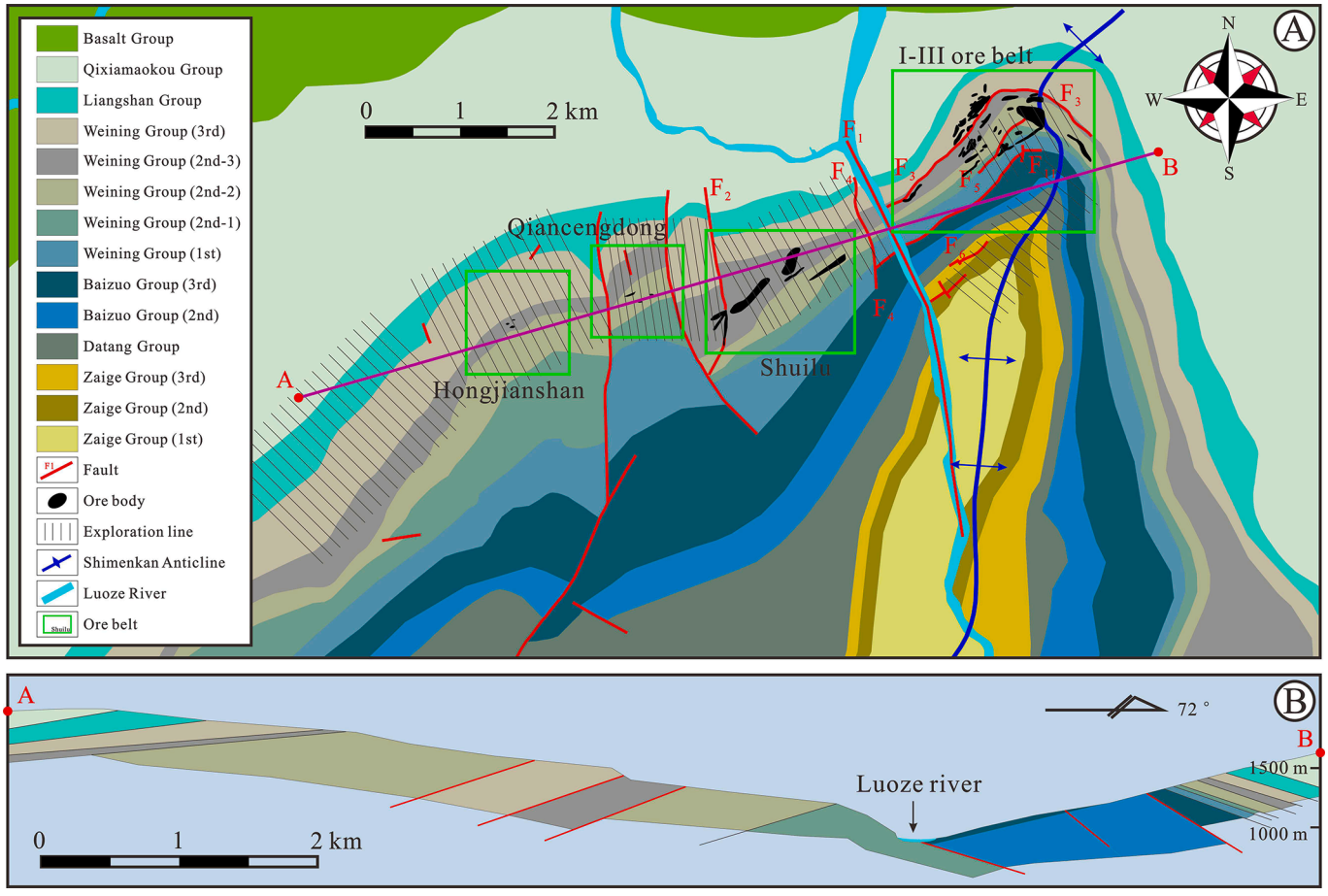

Fig. 2. Geological map of the Maoping Pb-Zn deposit, showing four ore belts of I-III, Shuilu, Qiancengdong and Hongjianshan, (B) Stratigraphic section of line A-B in the Maoping Pb-Zn deposit.

System	Series	Group	Section	Legend	Thickness (m)	Lithological characteristics	Orebody
Q					<10	Isabellinus alluvium, residual deluvium, sand gravel and clay	
Permian	Upper	Emeishan basalts			>400	LightGray and atrovirens amygdaloidal basalt	
	Lower	Qixia-Maokou Group			155-450	Upper: pewter grey middle-thick fine-grain limestone with asphaltene limestone Lower: gray thick-layer dense limestone containing biologicalfossils	
		Liangshan Group			21-45	Aubergine-beige sandstone and shale with bitumite of 0−5m, green middle−thick layer tuff and variegated calcareous breccia with 3−5 m from top to bottom	Bitumite
Carboniferous	Middle	Weining Group	3st		65-135	Gray−offwhite middle-thick fine-grain dolomite with white flint strips and lumps	
			2st-3		44-85	LightGray and offwhite middle-thick dolomite intercalated with limestone	Pb-Zn orebody: III, III-1, H-1, S-1
			2st-2		20-55	LightGray and offwhite middle-thick limestone with grey-green shale of 1−2 m in the middle−upper part and coarse-grained dolomite in the lower part	
			2st-1		15-50	Gray middle-thick fine-grain dolomite intercalated with limestone	
			1st		30-65	Gray, beige and ochre red middle−thick layer dolomite with fine−middle grain gray−green shale and straticulate biolimestone	
	Lower	Baizuo Group	3st		30-85	Upper: gray and steel gray middle-thick layer limestone of fine grain Lower: gray middle-thick layer argillaceous limestone with straticulate black shale	Pb-Zn orebody: II
			2st		25-70	Greyish-green and steel gray middle-thick layer limestone of fine grain with black flint strips and lumps	Pb-Zn orebody: II-1
		Datang Group			35-110	Greyish-green and black carbonate rocks, quartz sandstone with minor thin-bedded shale, and black shale with thin bedded sandstone	Anthracite
Devonian	Upper	Zaige Group	3st		9-40	Offwhite−gray middle-thick layer dolomite of coarse-grain with thin and carbonaceous shales of 1−2 cm	Pb-Zn orebody: I-9
			2st		52-70	Offwhite-gray thick-layer coarse-grain dolomite with light color algae-bearing dolomite and bits of shales	Pb-Zn orebody: I
			1st		>60	Offwhite thick-layer coarse-grain dolomite with straticulate carbonaceous shale	

Fig. 3. The stratagraphic histogram and ore body information of the Maoping Pb-Zn deposit.

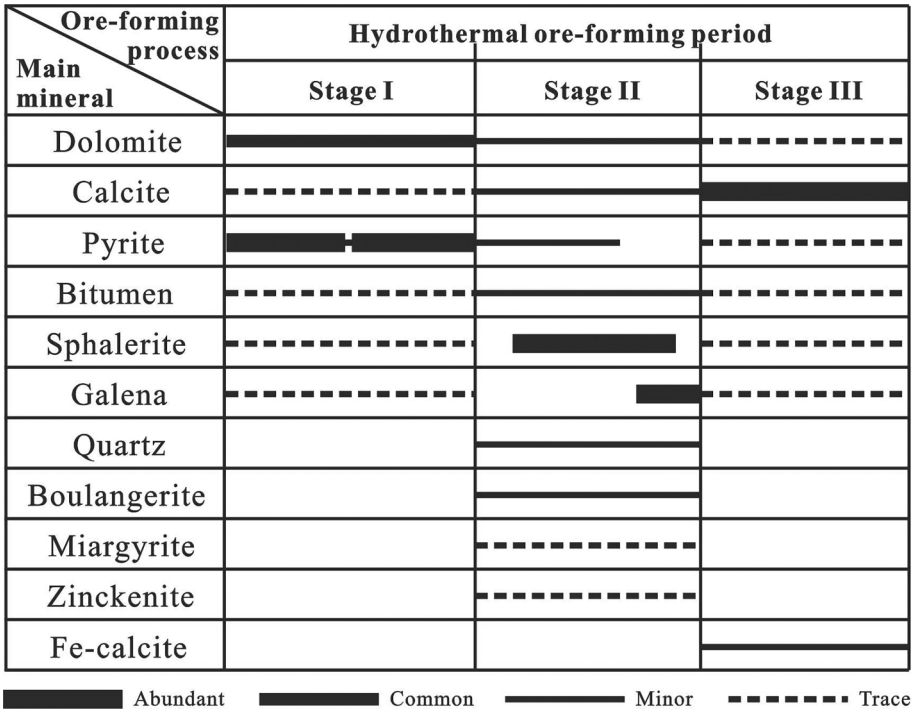

Fig. 4. Mineral sequence and paragenetic association of hydrothermal mineralization period in the Maoping Pb-Zn deposit.

"S" from north to south, indicating several late deformations (Fig. 2A). The Shimenkan anticline has a steep western limb with a dip of 65°–86°, while its eastern limb owns a gentler dip of 17°–35° (Wei et al., 2015). The strata from the core to the edge of the Shimenkan anticline are gradually younger, and the Emeishan basalts are only exposed in the northwest side of the Maoping deposit (Fig. 2B). A series of vertical faults and interbedded faults directly control the Pb-Zn ore body distribution in the western limb of the Shimenkan anticline. Among them, the former consists of F_1, F_2 and F_4 with NW-trending, and the later comprises F_3, F_5 and F_6 (Fig. 2A).

The mineral assemblage of hydrothermal alteration in the Maoping Pb-Zn deposit is relatively simple, namely early dolomite and late calcite alteration. Three hydrothermal stages (I, II, III) are distinguished in the deposit (Fig. 4). The dolomite + pyrite assemblages at stage I are distributed on the periphery of Pb-Zn mineralization and cut through the host carbonate rocks, containing rare galena and sphalerite (Supplementary Fig. 1A-C). Relative to the coarse dolomite veins at stage I, the dolomite content at stage II is significantly reduced, demonstrated by smaller dolomite veins (Supplementary Fig. 1D). In addition to the relatively pure galena and sphalerite at stage II, there are only small amounts of pyrite and boulangerite (Supplementary Fig. 1E, F). The veins at stage III are dominated by pure calcite, together with some hematite (Fig. 4G-I). The hydrothermal vein at stage II contains most of the sulfides (e.g., multi-color sphalerites, pyrite, galena, boulangerite; Fig. 5), and detailed mineral sequence and paragenetic association of three hydrothermal stages are presented in Fig. 4. The coarse-grained pyrite in stage I formed the earliest and was cut and replaced by fine-grained pyrite, sphalerite and galena at stage II (Fig. 6A, B). The galena and boulangerite post-dated the sphalerite and pyrite at stage II, and the calcite at stage III formed latest in the form of euhedral and heteromorphic structures (Fig. 6C, D).

3. Samples and analytical methods

3.1. Samples

The samples we collected were mainly from the No. I-III and Hongjianshan ore belts, including No. I-6, I-7, I-8, H-7 and H-8 ore bodies, which come from underground tunnel and drill cores. A total of 100 ore samples were used for this study. There are many colors of sphalerites during the mineralization stage (stage II), which are preliminarily classified as five colors: (C1) black, (C2) red brown, (C3) deep brown, (C4) light brown and (C5) light red. The close symbiotic relationship of black sphalerite and thick dolomite veins may represent an earlier formation sequence (Fig. 5A). C1 and C2 sphalerite are usually associated with each other (Fig. 5B), and C3 and C4 sphalerites often occur together in the form of C3 wrapping C4 (Fig. 5C). The C3 sphalerite occurs on the edge of C2, which are interspersed together with C4 (Fig. 5D). A sequence from C1 + C2 to C3 + C4 sphalerites appeared in turn between the pyrite vein (stage I) and the calcite vein (stage III) (Fig. 5E). There

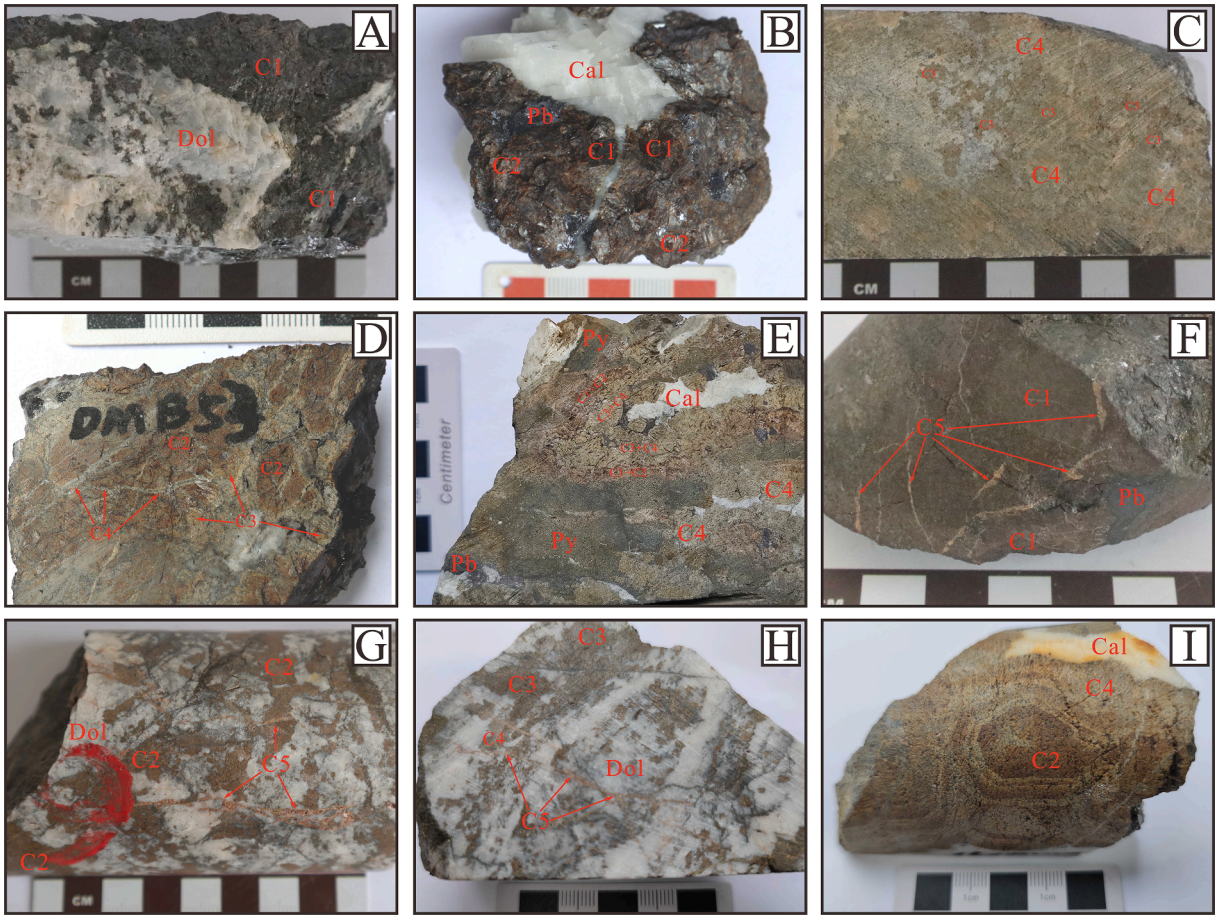

Fig. 5. Photos of different colors of sphalerite from the Maoping Pb-Zn deposit. (A) Black sphalerite (C1) associated with dolomite; (B) Symbiotic black (C1) and red brown sphalerite (C2), cut by late calcite veins; (C) Dark brown sphalerite (C3) coexists and predates the light brown sphalerite (C4); (D) The dark brown sphalerite (C3) occurs on the edge of red brown sphalerite (C2), which are cut by light brown sphalerite (C4); (E) A sequence from C1 + C2 sphalerite to C3 + C4 sphalerite appeared in turn between the pyrite vein at stage I and the calcite vein at stage III; (F-G) The light red sphalerite (C5) crosscutting the black (C1) and red brown sphalerite (C2); (H) The light red sphalerite (C5) veins in the dark brown (C3) and light brown sphalerite (C4); (I) Rhythmic variations from C2 sphalerite inside to C4 sphalerite outside. (For interpretation of the references to color in this figure legend, the reader is referred to the web version of this article.)

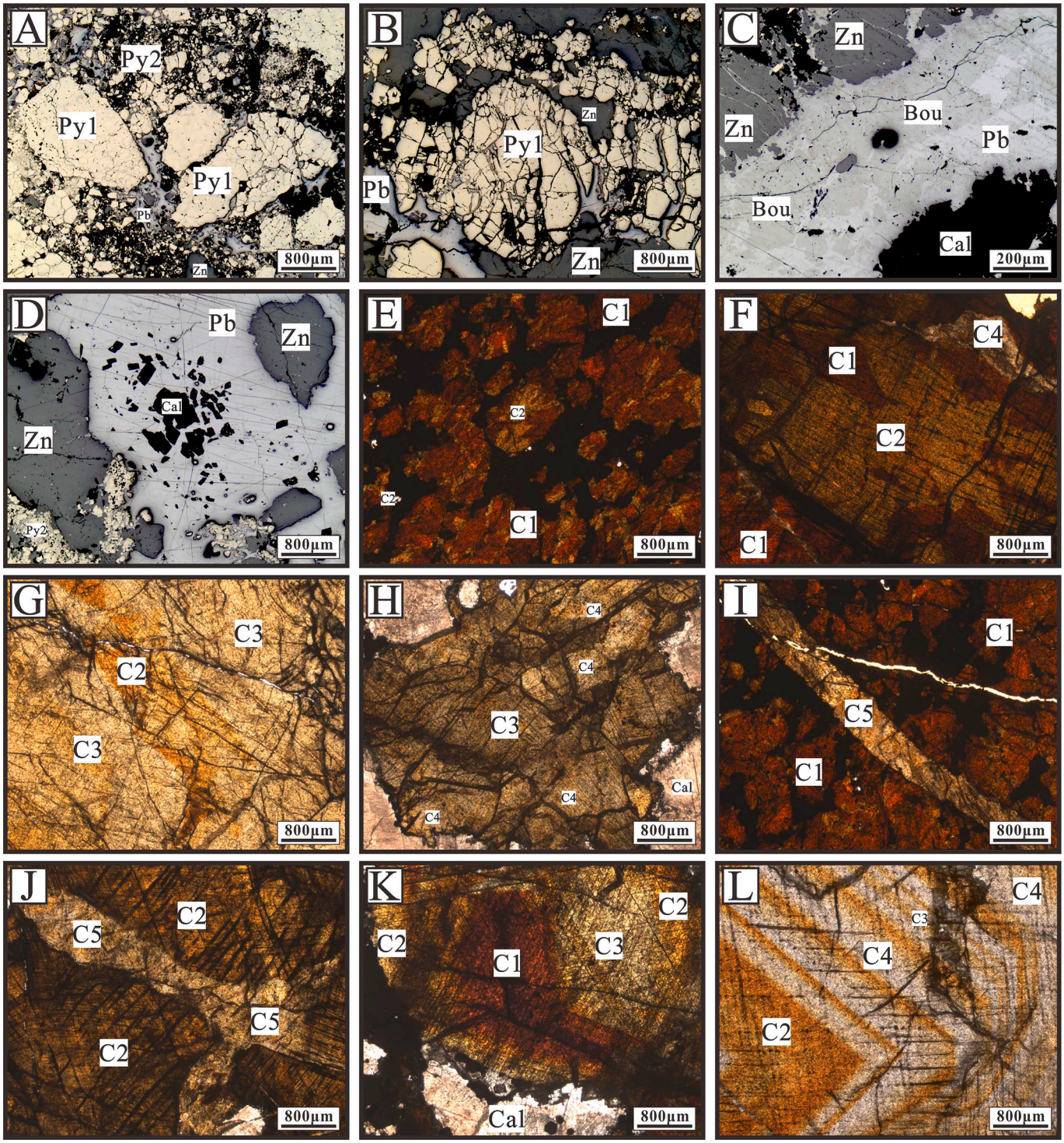

Fig. 6. (A-B) The coarse-grained pyrite (Py1) at stage I cut and replaced by the fine-grained pyrite-sphalerite-galena assemblage at stage II; (C) Galena and boulangerite cut the previous sphalerite and pyrite; (D) Euhedral calcite grains at stage III in galena; (E-F) Symbiotic C1 and C2 sphalerites are interspersed with veined C4 sphalerite; (G) C2 sphalerite veins cut C3 sphalerite; (H) C3 and C4 sphalerite assemblage; (I-J) C5 sphalerite as veins cut the C1 and C2 sphalerites, respectively; (K) Symbiotic C1, C2 and C3 sphalerites; (L) Rhythmic structure composed by C2, C3 and C4 sphalerites. Abbreviation: Py – "pyrite", Zn – "sphalerite", Pb – "galena", Bou – "boulangerite", Cal – "calcite", C1 – "black sphalerite", C2 – "red brown sphalerite", C3 – "dark brown sphalerite", C4 – "light brown sphalerite", C5 – "light red sphalerite". (For interpretation of the references to color in this figure legend, the reader is referred to the web version of this article.)

are some small C5 sphalerite veins in the C1 and C2 sphalerite, respectively (Fig. 5F, G), which also cross-cut the combination of C3 and C4 (Fig. 5H). Small amounts of sphalerites present rhythmic variations from C2 sphalerite inside to C4 sphalerite outside (Fig. 5I). Similar to the characteristics of hand specimens, the C1 and C2 sphalerites are often observed symbiotic under the microscope (Fig. 6E, F). The C3 sphalerite slightly post-dates C2, while C3 and C4 often coexist (Fig. 6G, H). The C1 and C2 sphalerites are interspersed by late C5 sphalerite veins, respectively (Fig. 6I, J). From the inside to the outside, sphalerite presents a transition change of C1 → C2 → C3, and a small amount of C2, C3 and C4 sphalerites formed rhythmic zonal structure (Fig. 6K, L). We grind typical sphalerite samples into laser sheets for further in-situ analysis.

We first selected the pure color areas for study, and the representative analyzed areas for each colored sphalerite are shown in the Supplementary Fig. 2A-E. In addition to pure colored sphalerite, we also analyzed sphalerite with rhythmic zone (i.e., Z1, Z2; Supplementary Fig. 2F-H).

3.2. Micro x-ray fluorescence (μ-XRF)

The μ-XRF analysis of sphalerite was carried out at Tuoyan Testing Technology Co., Ltd, Guangzhou, and the analyzed equipment is a M4 Plus micro x-ray fluorescence analyzer manufactured by German Bruker Company. A multiconductance capillary x-ray lens with a diameter of 20 μm as excitation light source has an operating power of 50 Kv and a current of 300 μA, equipped with two XFlash® silicon drift detector with a working air pressure of 2 Mbar (Sarjoughian et al., 2020). The generated x-rays can penetrate sample at depth ranging from a few microns to several hundred microns. The surface of the sample has been cleaned with an ear washing bulb or air gun prior to analysis, and then the analyzed sample is fixed to the objective table through metallographic plasticine. During the analysis, the sampling step is set to 20 μm and the single point residence time is set to 5 ms. The raw data is processed by M4 Tornado software to obtain the element mapping images (Agrosì et al., 2019). Ignoring the elements with poor signals, only the major Zn, S and Fe element mappings were exported.

3.3. Electron microprobe analysis (EMPA)

The major element compositions of sphalerite by EMPA were accomplished at the State Key Laboratory of Geological Processes and Mineral Resources, China University of Geosciences (Wuhan). First, we marked the analyzed area on the thin sections in order to easily find it under the microscope during analysis. Then the surface of sample section is sprayed with a thin carbon film, through a JEOL JEE-420 spraying carbon instrument (Zhang and Yang, 2016). The EMPA instrument is a JEOL JXA-8100 armed with four wavelength-dispersive spectrometers (WDS). The working parameters of the instrument are set as: (1) voltage of 15 KV, (2) current of 20 nA, (3) beam spot of 2 μm and (4) the background measurement time is half of the peak measurement time. The standard samples used include the American SPI mineral standards and the China National standards. The analyzed elements include Ge, Ga, S, Zn, Cu, Fe and Cd with detection limits of 0.01%, 0.01%, 0.01%, 0.05%, 0.02%, 0.02% and 0.01%, respectively, and the corresponding standard samples are germanium metal, gallium arsenide, sphalerite, sphalerite, cuprite, pyrite and cadmium metal, respectively. The peak and back analyzed time are 10 s and 5 s (Zn and S), 20 s and 10 s (Fe), and 30 s and 15 s (Ga, Ge, Cu and Cd), respectively. The precisions of the analyses were ±0.5% element concentrations. All original data before output report were matrix corrected on-line by a ZAF method.

3.4. Laser ablation inductively coupled plasma mass spectrometry (LA-ICP-MS)

The trace element analysis of sphalerite was carried out at Nanjing FocuMS Technology Co. Ltd, and the used LA-ICP-MS equipment was a 193 nm ArF excimer laser-ablation system (Analyte Excite) equipped with a quadrupole inductively coupled plasma mass spectrometry (Agilent 7700x) manufactured by the Agilent Technologies. The excimer laser generator can produce a deep ultraviolet beam with an energy density of ~6 J/cm^2, a beam spot diameter of 40 μm and a frequency of 6 Hz (Yu et al., 2019). Prior to formal analysis, all analyzed points were subjected to a brief laser pre-denudation to remove impurities or oxidized surface from the mineral. A complete analysis consists of 15 s of background signal collection and 40 s of sample signal collection, and the denuded samples were then mixed with helium and argon before being analyzed by ICP-MS. Elements to be monitored during analysis include Na^{23}, Mg^{25}, Al^{27}, Si^{29}, S^{34}, K^{39}, Ca^{42}, Sc^{45}, Ti^{47}, V^{51}, Cr^{53}, Mn^{55}, Fe^{57}, Co^{59}, Ni^{60}, Cu^{65}, Zn^{66}, Ga^{71}, Ge^{75}, As^{75}, Se^{77}, Rb^{85}, Sr^{88}, Y^{89}, Mo^{95}, Ag^{107}, Cd^{111}, In^{115}, Sn^{118}, Sb^{121}, Te^{125}, Cs^{133}, Ba^{137}, W^{182}, Tl^{205}, Bi^{209}, Pb^{Total}, Th^{232} and U^{238}. The USGS standard samples of MASS-1 and GSE-1G were used to calibrate the element content of sphalerite during the analysis. All raw data were processed offline by the ICPMSDataCal software, and the quantitative calculation of elements was completed by the method of Zn contents from EMPA as internal standard (Liu et al., 2008). The detection limit of most elements is better than 0.1 ppm, and the analyzed accuracy is higher than 20%.

The elemental mapping of sphalerite was accomplished at Analytical Laboratory of Nanjing FocuMS Technology Co. Ltd, using a laser denudation system of Photon-Machines Analyte HE equipped with the Agilent 7900 ICP-MS system. During the analysis, helium as a carrier gas and argon as a compensation gas is used to adjust sensitivity, together are combined into the ICP-MS. The laser surface scanning takes the laser line scanning as the unit, of which beam spot diameter is 15–40 μm, the denudation frequency is 10 Hz, and the denudation energy is 2–3 J/cm^2. Before and after the sample analysis, 30 s of background signal and 40 s of standard sample (NIST 610 and GSE-1G) denudation signal were collected respectively. Raw data is processed and imaged using the program LIMS SoftWare (based on Matlab), which can automatically complete the signal drift and background subtraction during analysis (e.g., Xiao et al., 2018).

3.5. Laser ablation multi-collector inductively coupled plasma mass spectrometry (LA-MC-ICP-MS)

The in-situ sulfur isotope analysis of sphalerite was completed at Ore Deposit Geochemistry Division, State Key Laboratory of Geological Processes and Mineral Resources, China University of Geosciences (Wuhan). The laser denudation system is Resonetics-S155 manufactured by Resolution Company, and its ArF excimer laser can emit a 193 nm deep ultraviolet beam that is focused on the mineral surface through a homogenized light path. The denudation process of a single point is about 40 s, and the parameters set include the beam spot diameter of 30 μm and denudation frequency of 5 Hz. High purity helium as carrier gas, mixed with argon and a small amount of nitrogen, together send the sample into the Nu Plasma II mass spectrometer. The standard samples used in the analysis are international sulfide standard NBS-123 and laboratory pyrite standard WS-1 (Zhu et al., 2017). After the analysis, we can directly obtain the $^{34}S/^{32}S$ ratios of the sample points and finally obtain the $\delta^{34}S$ value through standard-sample bracket method (SSB; Whitehouse et al., 2005; Niu et al., 2019). Based on the analysis of standards and replicate samples, the analytical error is estimated to be better than 0.1‰, and the instrument parameters, analytical conditions and operating procedures were consistent during the analysis season.

4. Results

4.1. Micro X-ray fluorescence (μ-XRF) of sphalerite

We selected two representative sphalerite samples with a variety of colors for micro x-ray fluorescence analysis, and analyzed major elements include Zn, S and Fe. The first sample (20MP-2-1) is a typical sphalerite with rhythmic zonation (Z1) and minor galena (Fig. 7A). The Zn and Fe signals in sphalerite have distinct rhythmic bands, consistent with the color of sphalerite, while the S signals do not change significantly throughout the sample (Fig. 7B-D). The sample 2 (20MP-44-1) comprises black (C1) and red brown (C2) sphalerite, cross-cut by light red (C5) sphalerite and pyrite veins (Fig. 7E). The C1 and C2 sphalerites show an orange Zn signals and dark blue Fe signals, while the C5 sphalerite reveals orange red Zn signals and black Fe signals (Fig. 7F, H). The C1, C2 and C3 sphalerites as a whole present unified green S signals, while the red sulfur signals correspond to the pyrite veins (Fig. 7G).

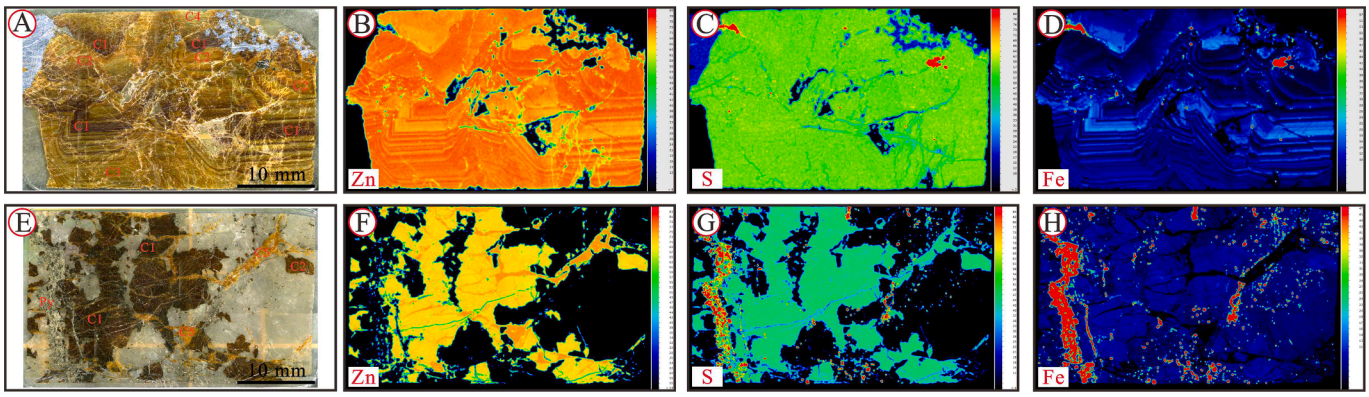

Fig. 7. Two analyzed samples showing the μ-XRF images (A, E), including Zn (B, F), S (C, G) and Fe (D, H) signals.

4.2. LA-ICP-MS element mapping of sphalerite

Two representative areas of sphalerite samples were used for LA-ICP-MS mapping analysis. The Sample 1 (20MP-2-1) is a typical sphalerite with rhythmic zonation (Fig. 8A, B), and these elements of Fe, Cu, Mn, Ag, Ga and Ge show significant signal changes (Fig. 8E-H, J, K). Among them, the Fe, Mn and Ga mappings have similar zonal characteristics, while the Cu and Ge share similar signals. The Ag, Cd, Sn and Sb exhibit certain changes in signal strengths, that have no obvious rule or connection, and the element signal of In can be ignored (Fig. 8I, L-N). The Sample 2 (20-MP-44-2) is C1 + C2 + C4 sphalerite cut by light red sphalerite vein (C5; Fig. 9A, B). There is no significant difference in the signal strength of Zn, S, In and Sb between C1 + C2 + C4 sphalerites and C5 sphalerite (Fig. 9C, D, L, N). While the former has enriched Fe, Mn, Ag and Sn and deficient Cu, Cd, Ga and Ge, conflicting with characteristics of C5 sphalerite (Fig. 9E-K, M).

4.3. Major and trace element compositions of sphalerite

A total of 344 points were subjected to analysis for major element compositions by EMPA, which are presented in Supplementary Table S1. Based on fifty data from two samples (20MP-70–1 and 20MP-72–1), the C1 sphalerite is composed of 58.20–62.29% Zn, 32.99–33.93% S and 4.25–7.98% Fe (Fig. 10A-C). Forty-six analyzed points demonstrate that the C2 sphalerite contains 63.58–65.03% Zn, 32.38–33.48% S and 2.11–3.29% Fe. The dominating Zn, S, Fe and Cd compositions in C3 sphalerite are 63.93–65.77%, 32.18–33.37%, 1.13–2.54% and 0.06–0.18%, respectively. The Zn, S and Fe contents of C4 sphalerite vary from 63.75 to 66.46%, 32.37–33.74% and 0.85–2.23%, respectively (Fig. 10A-C). The samples 20MP-44–1 and 20MP-44–2 confirm that the C5 sphalerite consists of 65.65–67.51% Zn and 32.07–33.44% S. Other element below 1% in C1 to C5 sphalerites and elemental contents of Z1 and Z2 sphalerites are summarized in Table S1. Based on Fe content (cut off at 1.0 %), the C1, C2, C3 and C4 sphalerites are classified

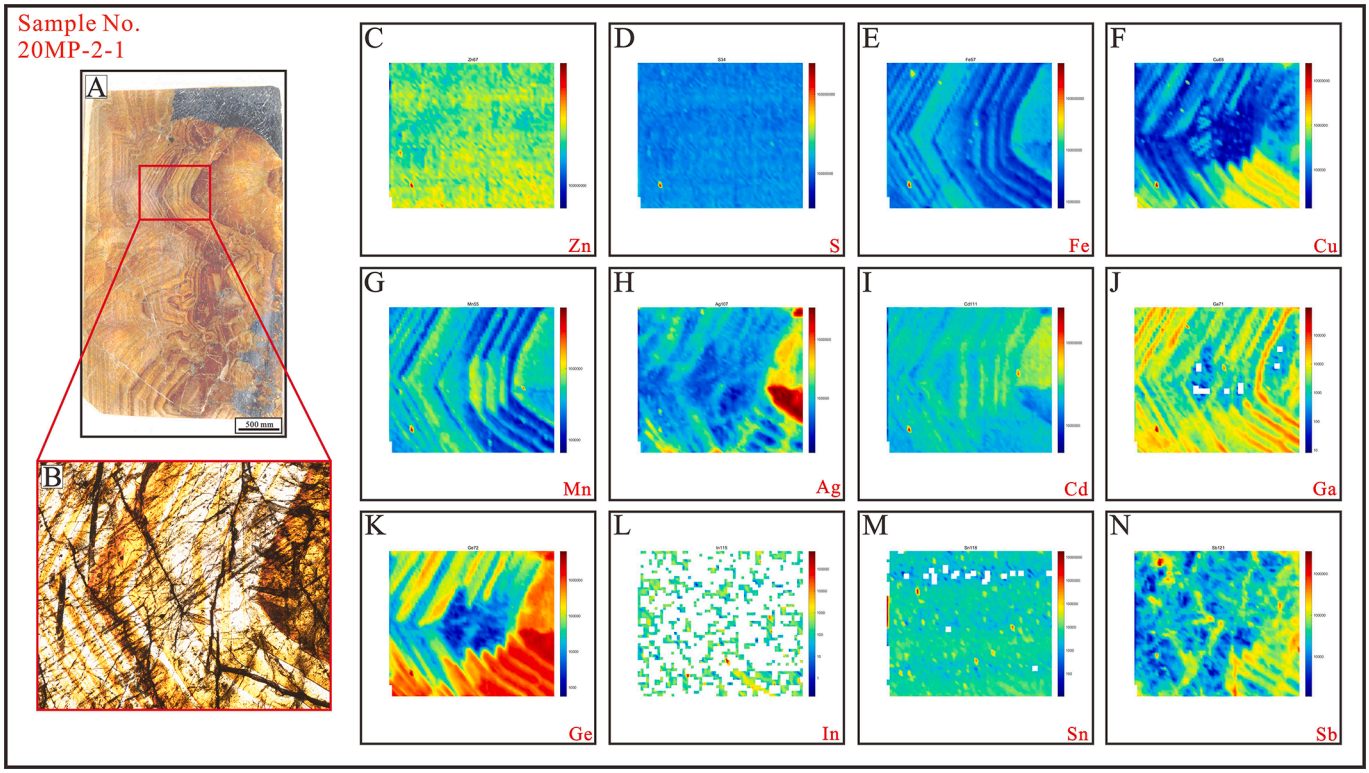

Fig. 8. The analyzed sphalerite sample (No. 20MP-2-1) by LA-ICP-MS, showing single polarized photo (A-B) and elemental signals for Zn, S, Fe, Cu, Mn, Ag, Cd, Ga, Ge, In, Sn and Sb (C-N).

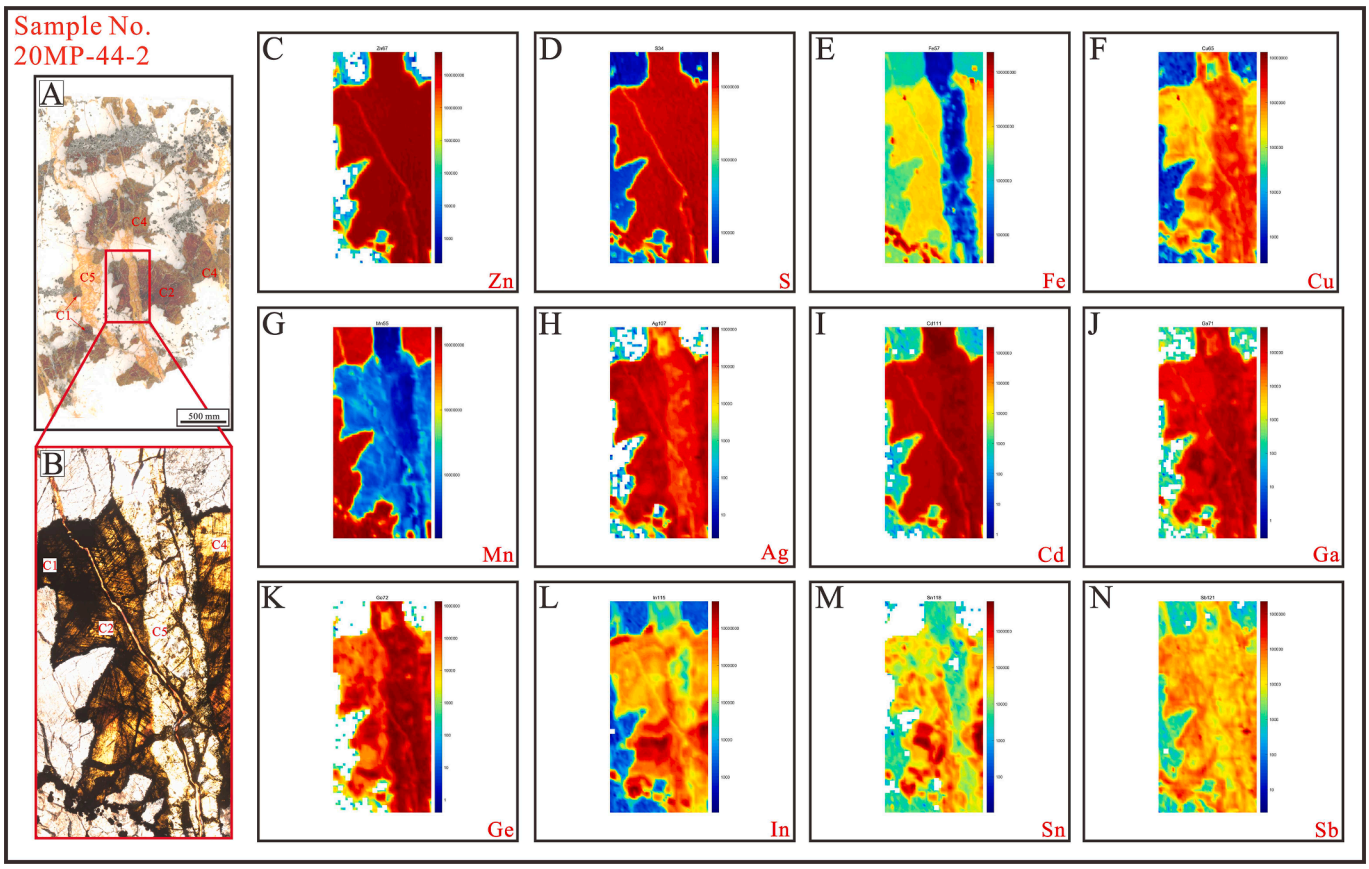

Fig. 9. The analyzed sphalerite sample (No. 20MP-44-2) by LA-ICP-MS, showing single polarized photo (A-B) and elemental signals for Zn, S, Fe, Cu, Mn, Ag, Cd, Ga, Ge, In, Sn and Sb (C-N).

as Fe-rich sphalerite and C5 as Fe-poor sphalerite in our subsequent discussion.

During laser ablation, most of trace elements exhibit smooth curve (Supplementary Fig. 3A-E). Few data for some elements reveal abrupt changes (e.g., Ca, Mg, Sr, Mn, Fe, Pb; Supplementary Fig. 3F, G), which has been removed to exclude the likely presence of mineral inclusions. Consistent with the analyzed point of the EMPA, we obtained 344 trace elements data of sphalerite by LA-ICP-MS (Table S2). The trace elements in significant amounts include Cd, Cu, Mn, Ge, Ga, As, Ag, Pb, Sb, In and Sn, all of which were corrected by Zn content of EMPA as an internal standard (Fig. 10D-N). The geometric mean is used to measure data of every element, but the arithmetic mean is used when the geometric mean is not applicable (Frenzel et al., 2016).

Cadmium: The highest levels of Cd (648–2305 ppm, geometric mean = 1214 ppm) are found in C5 sphalerite, and the Cd contents of 508–1372 ppm (geometric mean = 771 ppm) in C1 sphalerite take second place (Fig. 10D). The Cd contents are gradually increasing from C2 (388–724 ppm, geometric mean = 535 ppm), through C3 (516–1115 ppm, geometric mean = 637 ppm), to C4 sphalerite (611–1412 ppm, geometric mean = 797 ppm; Fig. 10D).

Copper: Similar to cadmium trend in different color sphalerites, highest Cu contents are determined in the C5 sphalerite (7–979 ppm, geometric mean = 242 ppm), followed by C4 sphalerite (19–253 ppm, geometric mean = 75 ppm). But the Cu contents of C1 (5–1081 ppm, geometric mean = 55 ppm), C2 (geometric mean = 27 ppm) and C3 (geometric mean = 23 ppm) sphalerites are relatively low (Fig. 10E).

Manganese: The Mn contents of 2–79 ppm (geometric mean = 50 ppm) in C1 sphalerite represents the maximum in the studied sphalerites, which exceed the C2 sphalerite of 17–40 (geometric mean = 27 ppm). The C3, C4 and C5 sphalerites contain 11–46 ppm, 12–93 ppm and 5–26 ppm Mn, respectively (Fig. 10F).

Germanium: The C5 and C1 sphalerites show distinct Ge contents of 1–195 ppm (geometric mean = 49 ppm) and 1–514 ppm (geometric mean = 22 ppm), respectively, in which several data of C1 sphalerite even show unusually high Ge contents of >200 ppm (Fig. 10G). The Ge contents of C2 and C3 sphalerites are low but C4 sphalerite contains some Ge composition (0–117 ppm, geometric mean = 13 ppm; Fig. 10G).

Arsenic: Only the C5 sphalerite contains a small amount of As (1–322 ppm, geometric mean = 68 ppm), and the As contents of C1, C2, C3 and C4 sphalerites are not apparent, in spite of several C1 and C2 sphalerite data containing As > 10 ppm (Fig. 10I).

Indium: Only the C2 and C5 sphalerites have significant indium contents of 0–175 ppm (geometric mean = 6 ppm) and 0–80 ppm (geometric mean = 9 ppm), respectively, and the amount of indium in C1, C3 and C4 sphalerite is extremely low (Fig. 10M).

Other trace element compositions of sphalerites are shown in Fig. 10J-M and summarized in Table S2. We selected the two most important components (PC1 and PC2) to represent the whole information of trace elements in sphalerite, constituting a binary diagram (Supplementary Fig. 4A-F).

4.4. Sulfur isotopes of sphalerite

A total of 144 *in-situ* sulfur isotope data were obtained from five colors of sphalerite (20 data each), which are presented in Fig. 11 and summarized in Table S3. The C1 sphalerite shows $\delta^{34}S$ values of 18.0–19.4‰, averaging 18.7‰, and the C2 sphalerite has $\delta^{34}S$ value of 19.1 to 20.0‰ (mean = 19.4‰). The $\delta^{34}S$ values of C3, C4 and C5 sphalerites are from 17.5 to 21.6‰, 17.6 to 21.9‰ and 15.6 to17.2‰, corresponding to average values of 19.9, 19.6 and 16.5‰, respectively (Fig. 11).

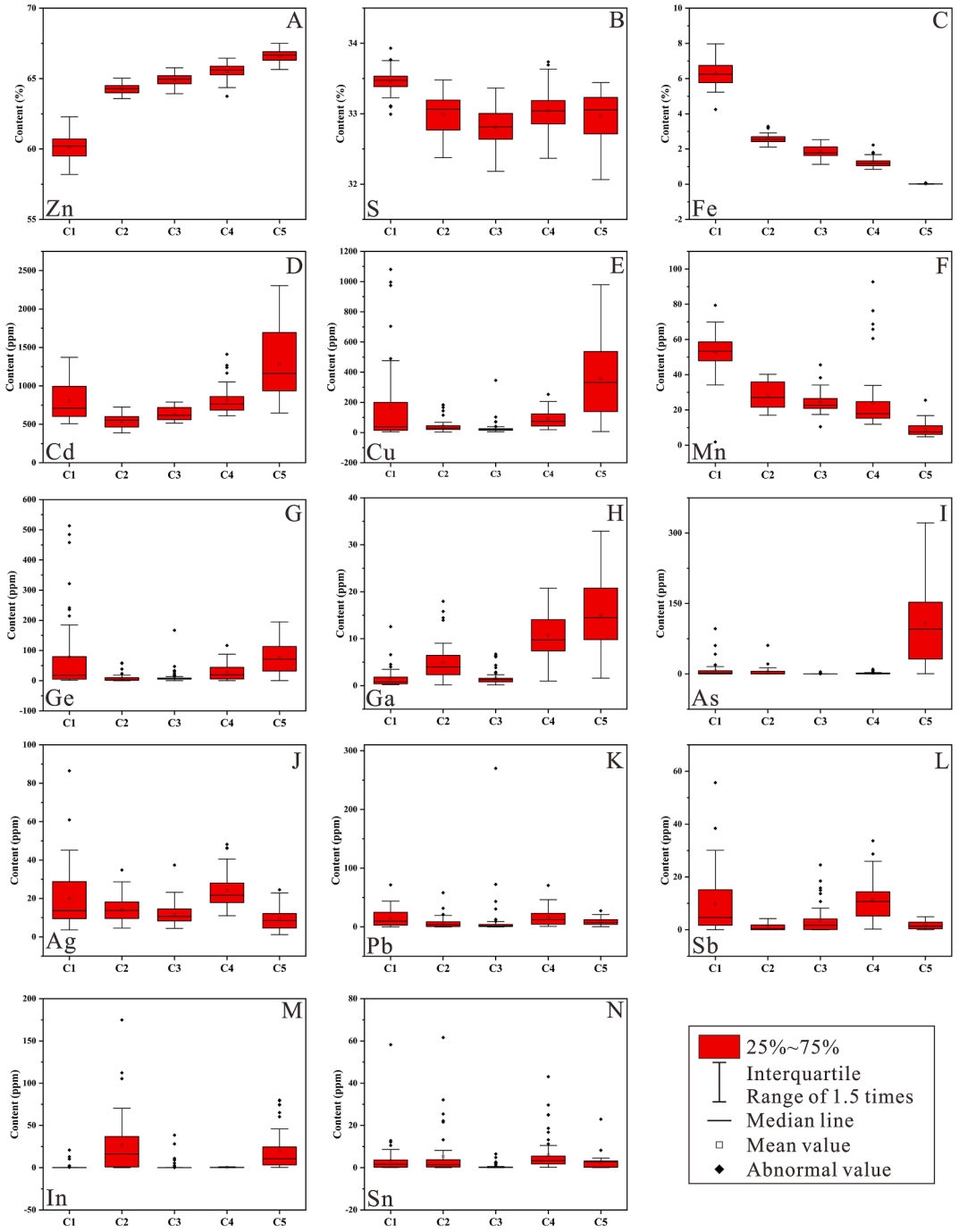

Fig. 10. Box-and-whisker diagrams of analyzed element contents of five colored sphalerites in the Maoping Pb-Zn deposit, with Zn, S, Fe contents (A-C) from EMPA data and other element (i.e., Cd, Cu, Mn, Ge, Ga, As, Ag, Pb, Sb, In, Sn) contents (D-N) from LA-ICP-MS data.

5. Discussion

5.1. Ge distribution and substitution mechanism

Although few independent minerals of germanium are found in many Pb-Zn polymetallic deposits, for example brunogeierite ($GeFe_2O_4$) and carboirite [$GeFeAl_2O_5(OH)_2$] (Arre Pb-Zn deposit, France); renierite ($Cu_{10}ZnGe_2Fe_4S_{16}$), germanite ($Cu_{13}Fe_2Ge_2S_{16}$) and briartite [$Cu_2(Fe, Zn)GeS_4$] (Tsumeb deposit in Namibia and Kipushi deposit in Zaire; Bernstein, 1985; Cugerone et al., 2019; Cugerone et al., 2021), none are found in the Maoping Pb-Zn deposit. Previous LA-ICP-MS studies have confirmed that germanium in sphalerite may exist in the form of solid solutions or nano-mineral inclusions (Gregory et al., 2015; Li et al., 2020; Fig. 12A-E), even if there are few data containing exceptionally high germanium contents (>200 ppm, Fig. 10G). In general, the C5 sphalerite has the highest germanium content (geometric mean = 49 ppm), followed by C1 sphalerite (geometric mean = 22 ppm).

The μ-XRF analysis and LA-ICP-MS spot analysis confirmed that Fe replacing Zn is the most important element substitution in the Maoping sphalerites (Fig. 7B, D, F, H; Fig. 12A). The Ge and Cu show similar signal change characteristics, which have nothing to the Fe signal in the LA-ICP-MS mapping (Fig. 8E, F, K; Fig. 9E, F, K). The PCA shows that Ge and Cu have very similar compositions in C1 and C5 sphalerites, which are not evident in other colored sphalerites (Supplementary Fig. 4A-E). Based on element contents, Cu and Ge are strongly correlated throughout all colored sphalerites, but the rate of the correlation is

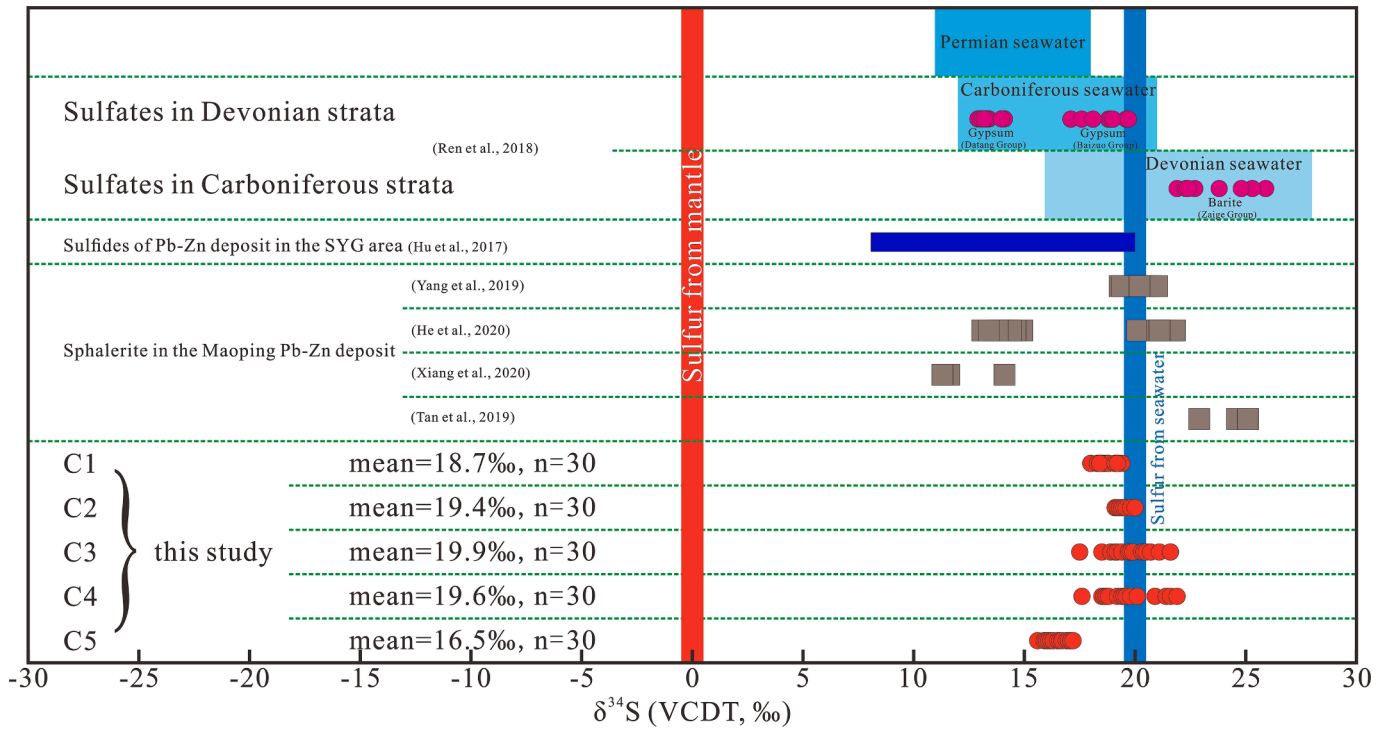

Fig. 11. Sulfur isotopic composition diagram of five colored sphalerites in the Maoping Pb-Zn deposit, also shown the previous published data for sphalerite of the Maoping deposit, sulfides of Pb-Zn deposit in the SYG area, sulfates in the peripheral Devonian and Carboniferous strata (data from Hu et al., 2017; Ren et al., 2018; Tan et al., 2019; Yang et al., 2019; He et al., 2020; Xiang et al., 2020).

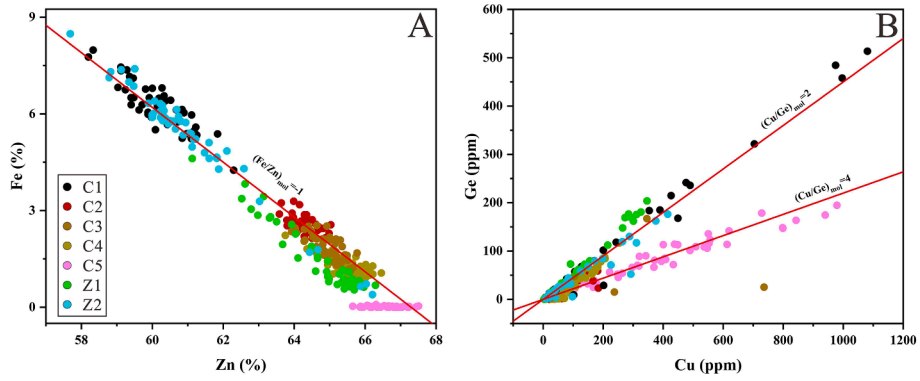

Fig. 12. Binary scatter plot of (A) Zn vs. Fe and (B) Cu vs. Ge from five colored and two zonal sphalerites in the Maoping Pb-Zn deposit, also shown the molar ratios between the elements.

clearly divided into two endmembers (Fig. 12B). The molar ratio of Cu to Ge is close to 4 in C5 sphalerite (Fe-poor), which approaches to 2 in other colored sphalerites (Fe-rich: C1, C2, C3, C4, Z1 and Z2; Fig. 12B). Hence, we propose the mechanism of $2Cu^{+} + Ge^{4+} \rightarrow 3Zn^{2+}$ in the Fe-rich sphalerites in the Maoping deposit, which has been widely demonstrated in other Pb-Zn deposits (e.g., Belissont et al., 2014; Yuan et al., 2018; Wei et al., 2019; Yu et al., 2021). The C5 sphalerite exhibits larger $(Cu/Ge)_{mol}$ ratios that may indicate a new Ge and Cu element coupling substitution, relative to $2Cu^{+} + Ge^{4+} \rightarrow 3Zn^{2+}$ in the Fe-rich sphalerites (Fig. 12B). However, compared with other colors of sphalerite, the C5 sphalerite has significantly higher arsenic levels, which is often found as nano-inclusions of sulfosalt (e.g., Cu-As-S, As-Sb-Pb-S) in sulfides (e.g., pyrite, chalcopyrite, sphalerite; Maske and Skinner, 1971; Orberger et al., 2003; Liu et al., 2021). In addition to As in C5 sphalerite, the amount of Ag and Ga increases linearly along with the Cu content, suggesting that a portion of Cu in C5 sphalerite may occur as nano-inclusion of Cu(Ag)-As(Ga)-S sulfosalt (Supplementary Fig. 5A-C), and Ge enters sphalerite in the same form of $2Cu^{+} + Ge^{4+} \rightarrow 3Zn^{2+}$ as other colored sphalerites. In general, the element substitution of Ge for all colored sphalerites is $2Cu^{+} + Ge^{4+} \rightarrow 3Zn^{2+}$, while the nano-inclusions of Cu(Ag)-As(Ga)-S sulfosalt are evenly distributed in C5 sphalerite that results in its higher $(Cu/Ge)_{mol}$ ratios (4 but 2 based on $2Cu^{+} + Ge^{4+} \rightarrow 3Zn^{2+}$).

5.2. *Enrichment factor of germanium*

Previous experiments confirmed that the content of germanium in ore-forming fluid is the main factor controlling germanium enrichment, which can directly affect the amount of germanium entering sphalerite during ore precipitation process (Liang et al., 2009). In addition to the fluid properties, the physicochemical conditions during mineralization also command the enrichment of germanium. Based on the content of Fe and FeS activity in sphalerite, we calculated the ore-forming temperature and sulfur fugacity, respectively (Fig. 13; Keith et al., 2014; Frenzel

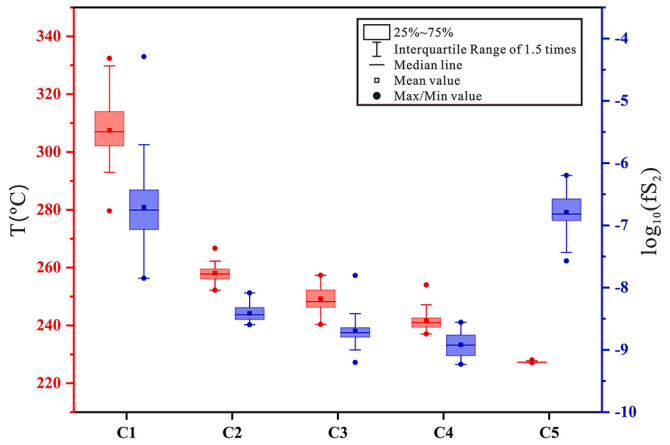

Fig. 13. Box-and-whisker diagrams of calculated temperature (A) and sulfur fugacity (B) from five colored sphalerites in the Maoping Pb-Zn deposit (data calculated after Keith et al., 2014; Frenzel et al., 2021).

et al., 2021). The ore-forming temperature of C1 sphalerite ranges from 280 to 332 °C, representing the highest ore-forming temperature in the studied sphalerites, of which in C2 (252–267 °C), C3 (240–257 °C), C4 (237–254 °C) and C5 (227–228 °C) sphalerites are gradually decreasing, respectively (Fig. 13). By microthermometry, the homogenization temperature of fluid inclusions in sphalerite is in the range of 104–351 °C and concentrated at 200–300 °C, the highest temperature of which is similar to the calculated highest ore-forming temperature (332 °C) with the Fe/Zn geothermometer, while the calculated minimum ore-forming temperature (227 °C) is about 100 °C higher than the homogenization temperature, showing that there will be a large error in low-temperature range based on Fe/Zn geothermometer (Keith et al., 2014; Han et al., 2019). The C1 and C5 sphalerites have the highest sulfur fugacity ($\log_{10}fS_2$), followed by the C2, C3 and C4 sphalerites. The sequence of C1 → C2 → C3 → C4 has the decreasing $\log_{10}fS_2$, suggesting that the decreasing tendency of reduced sulfur content (S^{2-}), while a sudden increase in sulfur fugacity of C5 sphalerite can be recognized (Fig. 13). The C1 and C5 sphalerites have the highest germanium content, consistent with their higher sulfur fugacity, relative to C2, C3 and C4 sphalerites (Fig. 10G; Fig. 13), implying that sulfur fugacity, not temperature, is the most important factor controlling the content of germanium in sphalerite (Borojević et al., 2011; Keith et al., 2014; Sun et al., 2019). The hydroxide ($Ge(OH_4)$) and chloride ($GeCl_4$) are the two main germanium transported species in aqueous hydrothermal fluids (Pokrovski and Schott, 1998; Höll et al., 2007; Mare et al., 2020). Because of TSR and BSR, the sulfate in the fluid was continuously converted to reduced sulfur (S^{2-}), hence higher sulfur fugacity means higher reduced sulfur contents (Worden et al., 1995; Leach et al., 2005; Zhou et al., 2018). Higher S^{2-} content will bind H^+ in the fluid (e.g., HS^-, H_2S, HCl), resulting in higher pH and increasing $Ge(OH)_4/GeCl_4$ contents in hydrothermal fluids in view of $Ge^{4+} + 4OH^- \leftrightarrow Ge(OH)_4$ and $Ge^{4+} + 4Cl^- \leftrightarrow GeCl_4$ (Wood and Samson, 2006).

5.3. Two-stage enrichment of germanium

Based on the obvious crosscutting relationship between C5 sphalerite and other colored sphalerites, we propose that C1, C2, C3 and C4, together with their rhythmic band sphalerites (i.e., Z1 and Z2), and C5 sphalerite were derived from different ore-forming fluids (Fig. 5F-H; Supplementary Fig. 2A, E). As the important metal-bearing strata, the Devonian Baizuo Formation and Carboniferous Zaige Formation host gypsum and barite with the $\delta^{34}S$ values of +18.8 to +25.9‰, similar to the values of C1 to C4 sphalerite (18.0–21.9‰), and this suggests that the reduced sulfur in C1 to C4 sphalerites came from the surrounding Baizuo and Zaige Formations (Fig. 11; Ren et al., 2018). From C1 and C2 to C3 and C4 sphalerites, their $\delta^{34}S$ variation (C1 and C2: $\delta^{34}S_{max\text{-}min} <$ 1.5‰; C3 and C4: $\delta^{34}S_{max\text{-}min} <$ 4.3‰) gradually increase, and decreasing temperature of ore-forming fluid temperature can promote bacterial sulfate reduction (BSR) and restrain thermochemical sulfate reduction (TSR; Fig. 11; Fig. 13; Henjes-Kunst et al., 2017; Slack et al., 2019). The sulfur in C5 sphalerite exhibits lower $\delta^{34}S$ value (15.6 to17.2‰) with more limited variation, suggesting that the sulfur in C5 sphalerite derived from Carboniferous Datang Formation (Fig. 11). This conclusion can be also explained by the significantly lower ore-forming temperature and suddenly increasing sulfur fugacity of C5 sphalerite, compared with other colored sphalerites (Fig. 13; Ren et al., 2018; He et al., 2020; Xiang et al., 2020). Given that the mixing of reduced-sulfur fluid and metal-bearing (Pb, Zn, Ag) basin brine is the main ore-forming mechanism in the Maoping Pb-Zn deposit, we suggest that germanium mainly occurs in reduced-sulfur fluid in the form of $Ge(OH)_4$ or $GeCl_4$ from surrounding strata (e.g., Zaige, Baizuo and Datang Formations) rather than the oxidizing metal-bearing fluids (Zhou et al., 2018; Wu et al., 2021). Based on the chalcophile and organophilic affinities of germanium, the black shale with a large proportion in the Datang Formation may provide more germanium sources than the Zaige and Baizuo Formations, which are dominated by carbonate rocks (dolomite and limestone; Fig. 3; Höll et al., 2007; Yang et al., 2019). In addition, the extensive coal mines (e.g., anthracite) in the Datang Formation are also potential sources of germanium (Fig. 3; Rosenberg, 2008; Xiang et al., 2020). It is noteworthy that few sandstone and shale interlayers in the Zaige and Baizuo Formations may be the source of germanium in C1-C4 sphalerites, given the lower Clark values of carbonate rocks (0.2 ppm) than sandstone (0.8 ppm) and shale (1.6 ppm; Fig. 3; Faure, 1998). In general, the black shale or sandstone interlayers in these strata (e.g., Zaige, Baizuo and Datang Formations) may be the source of germanium in the Maoping deposit, which were extracted and leached to complete the germanium migration from organic complex to hydrothermal fluid during the formation of the fluid containing reduced sulfur (Wood and Samson, 2006; Rosenberg, 2008). Therefore, the two-stage enrichment process of germanium in the Maoping Pb-Zn deposit can be summarized as follows: (1) the metal-bearing basin brine first entered the Zaige and Baizuo Formations and mixed with the internal germanium-bearing reduced-sulfur fluid to precipitate C1, C2, C3, C4 and some rhythmic band sphalerites (i.e., Z1 and Z2); (2) The germanium-bearing reduced-sulfur fluid in the Datang Formation moved to the Zaige and Baizuo Formations and continued to mix with the remaining metal-bearing basin brine, and then the C5 sphalerite precipitated.

6. Conclusions

(1) Five colors of sphalerite were identified in the Maoping Pb-Zn deposit, including (C1) black, (C2) red brown, (C3) deep brown, (C4) light brown and (C5) light red sphalerite, in which C5 sphalerite clearly is crosscutting other colored sphalerites.
(2) The C5 sphalerite has the highest germanium content (mean: 49 ppm), followed by C1 sphalerite (mean: 22 ppm), and the Ge contents of C2 and C3 sphalerites are low but C4 sphalerite contains some Ge composition (mean: 13 ppm).
(3) Germanium incorporates into all colored sphalerites via $2Cu^+ + Ge^{4+} \rightarrow 3Zn^{2+}$, and the nano-inclusions of Cu(Ag)-As(Ga)-S sulfosalt evenly distributed in C5 sphalerite result in its higher $(Cu/Ge)_{mol}$ ratios.
(4) Sulfur fugacity, rather than temperature, placed the dominant control on the enrichment of germanium in sphalerite.
(5) The mixing between the metal-bearing basin brine and fluids with germanium and reduced-sulfur derived from the Zaige and Baizuo Formations caused the first germanium enrichment, and the fluid with germanium and reduced-sulfur derived from the Datang Formation took responsibility for the second enrichment of germanium.

Declaration of Competing Interest

The authors declare that they have no known competing financial interests or personal relationships that could have appeared to influence the work reported in this paper.

Data availability

All data are included in the paper as Supplementary tables

Acknowledgments

We appreciate Mr. Xiao Yang, Zhu Peng and Guo Tengda for their help during analyses. This study is financially supported by grants from the National Key Research and Development Program of China (2021YFC2900300), the National Natural Science Foundation of China (No. 92162323), the Fundamental Research Funds for National Universities, China University of Geosciences (Wuhan), and the program of China Scholarships Council (No. 202106410073). The manuscript was significantly improved through two anonymous reviewers.

Appendix A. Supplementary data

Supplementary data to this article can be found online at https://doi.org/10.1016/j.oregeorev.2023.105421.

References

Agrosì, G., Tempesta, G., Mele, D., Caggiani, M.C., Mangone, A., Ventura, G.D., Cestelli-Guidi, M., Allegretta, I., Allegretta, M.T., Nimis, P., Nimis, F., 2019. Multiphase inclusions associated with residual carbonate in a transition zone diamond from Juina (Brazil). Lithos 350–351, 105279.

Bauer, M.E., Burisch, M., Ostendorf, J., Krause, J., Frenzel, M., Seifert, T., Gutzmer, J., 2019. Trace element geochemistry of sphalerite in contrasting hydrothermal fluid systems of the Freiberg district, Germany: insights from LA-ICP-MS analysis, near-infrared light microthermometry of sphalerite-hosted fluid inclusions, and sulfur isotope geochemistry. Miner. Deposita 54, 237–262.

Belissont, R., Boiron, M.C., Luais, B., Cathelineau, M., 2014. LA-ICP-MS analysis of minor and trace elements and bulk Ge isotopes in zoned Ge-rich sphalerited from the Noailhac-Saint-Salvy deposit (France): insights into incorporation mechanisms and ore deposition process. Geochim. Cosmoc. Acta 126, 518–540.

Belissont, R., Munoz, M., Boiron, M.C., Luais, B., Mathon, O., 2016. Distribution and oxidation state of Ge, Cu and Fe in sphalerite by l-XRF and K-edge l-XANES: insights into Ge incorporation, partitioning and isotopic fractionation. Geochim. Cosmoc. Acta 177, 298–314.

Bernstein, L R, 1985. Germanium geochemistry and mineralogy. Geochim. Cosmochim. Acta 49, 2409–2422.

Bonnet, J., Mosser-Ruck, R., André-Mayer, A.S., Jean, C., Bailly, L., 2014. Germanium distribution in sphalerite from north-east America MVT deposits: A multiscale study. Acta Geol. Sin. 88 (supp. 2), 437–439.

Borojević, Šoštarić, S., Palinkaš, L.A., Topa, D., Spangenberg, J.E., Prochaska, W., 2011. Silver–base metal epithermal vein and listwaenite types of deposit Crnac, Rogozna Mts, Kosovo. Part I: Ore mineral geochemistry and sulfur isotope study. Ore Geol. Rev. 40, 65–80.

Chihong Mining Co., LTD, 2018. The resource reserve verification report of the Maoping Pb-Zn deposit. Internal Report 1–106 (in Chinese).

Cook, N.J., Ciobanu, C.L., Pring, A., Skinner, W., Shimizu, M., Danyushevsky, L., Saini-Eidukat, B., Melcher, F., 2009. Trace and minor elements in sphalerite: A LA-ICP-MS study. Geochim. Cosmoc. Acta 73, 4761–4791.

Cook, N.J., Etschmann, B., Ciobanu, C.L., 2015. Distribution and substitution mechanism of Ge in a Ge-(Fe)-bearing sphalerite. Minerals 5, 117–132.

Cugerone, A., Cenki-Tok, B., Oliot, E., Muñoz, M., Barou, F., Motto-Ros, V., Goff, E.L., 2019. Redistribution of germanium during dynamic recrystallization of sphalerite. Geology 48, 236–241.

Cugerone, A., Cenki-Tok, B., Muñoz, M., Kouzmanov, K., Oliot, E., Motto-Ros, V., Goff, E. L., 2021. Behavior of critical metals in metamorphosed Pb-Zn ore deposits: example from the Pyrenean Axial Zone. Miner. Deposita 6, 685–705.

Faure, G., 1998. Principles and Applications of Geochemistry, second ed. Prentice Hall, New Jersey. pp. 1−928.

Frenzel, M., Hrisch, T., Gutzmer, J., 2016. Gallium, germanium, indium, and other trace and minor elements in sphalerite as a function of deposit type-a meta-analysis. Ore Geol. Rev. 76, 52–78.

Frenzel, M., Voudouris, P., Cook, N.J., Ciobanu, C.L., Gilbert, S., Wade, B.P., 2021. Evolution of a hydrothermal ore-forming system recorded by sulfide mineral chemistry: a case study from the Plaka Pb–Zn–Ag deposit, Lavrion, Greece. Miner. Deposita 57, 417–438.

Gregory, D.D., Large, R.R., Halpin, J.A., Baturina, E.L., Lyons, T.M., Wu, S., Danyushevsky, L., Sack, P.J., Chappaz, A., Maslennikov, V.V., Bull, S.W., 2015. Trace element content of sedimentary pyrite in black shales. Econ. Geol. 110, 1389–1410.

Han, R.S., Liu, C.Q., Huang, Z.L., Chen, J., Ma, D.Y., Lei, L., Ma, G.S., 2007. Geological features and origin of the Huize carbonate-hosted Zn-Pb-(Ag) district, Yunnan, South China. Ore Geol. Rev. 31, 360–383.

Han, R.S., Chen, J., Wang, F., Wang, X.K., Li, Y., 2015. Analysis of metal-element association halos within fault zones for the exploration of concealed ore-bodies -A case study of the Qilinchang Zn-Pb-(Ag-Ge) deposit in the Huize mine district, northeastern Yunnan, China. J. Geochem. Explor. 159, 62–78.

Han, R.S., Zhang, Y., Wang, F., Wu, P., Qiu, W.L., Li, W.Y., 2019. Metallogenicmechanism and location prediction of concealed ore bodies of Germanium-rich silver-zinc-lead deposits in the polymetallic deposit concentrated district in. Beijing, China Science Press, Northeastern Yunnan, China, pp. 1–510 (in Chinese).

He, Y.F., Wu, T., Huang, Z.L., Ye, L., Deng, P., Xiang, Z.Z., 2020. Genesis of the Maoping carbonate-hosted Pb-Zn deposit, northeastern Yunnan Province, China: evidences from geology and C-O-S-Pb isotopes. Acta Geochim. 39, 782–796.

Henjes-Kunst, E., Raith, J.G., Boyce, A.J., 2017. Micro-scale sulfur isotope and chemical variations in sphalerite from the Bleiberg Pb-Zn deposit, Eastern Alps, Austria. Ore Geol. Rev. 90, 52–62.

Höll, R., Kling, M., Schroll, E., 2007. Metallogenesis of germanium—A review. Ore Geol. Rev. 30, 145–180.

Hu, R.Z., Fu, S.L., Huang, Y., Zhou, M.F., Fu, S.H., Zhao, C.H., Wang, Y.J., Bi, X.W., Xiao, J.F., 2017. The giant South China Mesozoic low-temperature metallogenic domain: Reviews and a new geodynamic model. J. Asian Earth. Sci. 137, 9–34.

Hu, Y.S., Wei, C., Huang, Z.L., Danyushevsky, L., Wang, H.Y., 2021. LA-ICP-MS sphalerite and galena trace element chemistry and mineralization-style fingerprinting for carbonate-hosted Pb-Zn deposits: Perspective from early Devonian Huodehong deposit in Yunnan, South China. Ore Geol. Rev. 136, 104253.

Keith, M., Haase, K.M., Schwarz-Schampera, U., Klemd, R., Petersen, S., Bach, W., 2014. Effects of temperature, sulfur, and oxygen fugacity on the composition of sphalerite from submarine hydrothermal vents. Geology 42, 699–702.

Kong, Z.G., Wu, Y., Liang, T., Zhang, F., Meng, X.Y., Lu, L., 2018. Sources of ore-forming material for Pb-Zn deposits in the Sichuan-Yunnan-Guizhou triangle area: Multiple constraints from C-H-O-S-Pb-Sr isotopic compositions. Geol. J. 53, 159–177.

Leach, D.L., Sangster, D.F., Kelley, K.D., 2005. Sediment-hosted lead-zinc deposits: a global perspective. Econ. Geol. 100th Anniversary 561–607.

Li, Z.L., Ye, L., Hu, S.Y., Wei, C., Huang, Z.L., Yang, Y.L., Danyushevsky, L., 2020. Trace elements in sulfides from the Maozu Pb-Zn deposit, Yunnan Province, China: Implications for trace-element incorporation mechanisms and ore genesis. Am. Mineral. 105, 1734–1751.

Liang, Y.Q., Wang, J.K., Yan, J.F., Liao, W.X., 2009. Low and medium temperature pressure oxidation leaching of Germanium-rich sphalerite concentrate. Nonferrous Met. 61 (3), 62–70 (in Chinese with English abstract).

Liu, H.C., Lin, W.D., 1999. Study on the law of Pb-Zn-Ag Ore deposit in Northeast Yunnan, China. Yunnan University Press, Kunming 1-468 (in Chinese).

Liu, Y.S., Hu, Z.C., Gao, S., Günther, D., Xu, J., Gao, C.G., Chen, H.L., 2008. In situanalysis of major and trace elements of anhydrous minerals by LA-ICP-MS without applying an internal standard. Chem. Geol. 257, 34–43.

Liu, Y.F., Qi, H.W., Bi, X.W., Hu, R.Z., Qi, L.K., Yin, R.S., Tang, Y.Y., 2021. Two types of sediment-hosted Pb-Zn deposits in the northern margin of Lanping basin, SW China: Evidence from sphalerite trace elements, carbonate C-O isotopes and molybdenite Re-Os age. Ore Geol. Rev. 131, 104016.

Liu, S., Zhang, Y., Ai, G.L., Xue, X.L., Li, H.B., Shah, S.A., Wang, N.H., Chen, X., 2022. LA-ICP-MS trace element geochemistry of sphalerite: Metallogenic constraints on the Qingshuitang Pb–Zn deposit in the Qinhang Ore Belt, South China. Ore Geol. Rev. 141, 104659.

Liu, T.T., Zhu, C.W., Yang, G.S., Zhang, G.S., Fan, H.F., Zhang, Y.X., Wen, H.J., 2020. Primary study of germanium isotope composition in sphalerite from the Fule Pb-Zn deposit, Yunnan province. Ore Geol. Rev. 120, 103466.

Luo, K., Cugerone, A., Zhou, M.F., Zhou, J.X., Sun, G.T., Xu, J., He, K.J., Lu, M.D., 2022. Germanium enrichment in sphalerite with acicular and euhedral textures: an example from the Zhulingou carbonate-hosted Zn(-Ge) deposit, South China. Miner. Deposita 57, 1343–1356.

Mare, E.R., O'Neill, H.S.C., Berry, A.J., Glover, C.J., 2020. The stability of divalent Ge in silicate melts and its geochemical properties. Chem. Geol. 532, 119306.

Maske, S., Skinner, B.J., 1971. Studies of the sulfosalts of copper; I, Phases and phase relations in the system Cu-As-S. Econ. Geol. 66, 901–918.

Melcher, F., Buchholz, P., 2014. Germanium. Critical Metals Handbook 177–203.

Meng, Q.R., Zhang, G.W., 2000. Geologic framework and tectonic evolution of the Qinling orogen, central China. Tectonophysics 323, 183–196.

Mishra, B.P., Pati, P., Dora, M.L., Baswani, S.R., Meshram, T., Shareef, M., Pattanayak, R. S., Suryavanshi, H., Mishra, M., Raza, M.A., 2021. Trace-element systematics and isotopic characteristics of sphalerite-pyrite from volcanogenic massive sulfide deposits of Betul belt, central Indian Tectonic Zone: Insight of ore genesis to exploration. Ore Geol. Rev. 134, 104149.

Niu, P.P., Jiang, S.Y., Xiong, S.F., Hu, Q.S., Xu, T.L., 2019. Geological characteristics, fluid inclusions and H-O-C-S isotopes of the Zaopa Ag-Mo prospect in the Suizao area, Hubei Province: Implications for ore genesis. Ore Geol. Rev. 111, 103012.

Orberger, B., Pasava, J., Gallien, J.P., Daudin, L., Trocellier, P., 2003. Se, As, Mo, Ag, Cd, In, Sb, Pt, Au, Tl, Re traces in biogenic and abiogenic sulfides from Black Shales (Selwyn Basin, Yukon territories, Canada): A nuclear microprobe study. Nucl. Instrum. Meth. B 210, 441–448.

Pfaff, K., Koenig, A., Wenzel, T., Ridley, I., Hildebrandt, L.H., Leach, D.L., Markl, G., 2011. Trace and minor element variations and sulfur isotopes in crystalline and

colloform ZnS: Incorporation mechanisms and implications for their genesis. Chem. Geol. 286, 118–134.
Pokrovski, G.S., Schott, J., 1998. Thermodynamic properties of aqueous Ge(IV) hydroxide complexes from 25 to 350 °C: implications for the behaviour of germanium and the Ge/Si ratio in hydrothermal fluids. Geochim. Cosmoc. Acta 62, 1631–1642.
Ren, S.L., Li, Y.H., Zeng, S., Qiu, W.L., Fan, C.F., Hu, G.Y., 2018. Effect of sulfateevaporate salt layer in mineralization of the Huize and Maoping lead-zinc deposits in Yunnan: evidence from sulfur isotope. Acta Geol. Sin. 92, 1041–1055 (in Chinese with English abstract).
Rosenberg, E., 2008. Germanium: Environmental occurrence, importance and speciation. Rev. Environ. Sci. Bio. 8, 29–57.
Sarjoughian, F., Habibi, I., Lentz, D.R., Azizi, H., Esna-Ashari, A., 2020. Magnetite compositions from the Baba Ali iron deposit in the Sanandaj-Sirjan zone, western Iran: Implications for ore genesis. Ore Geol. Rev. 126, 103728.
Shanks, W. C. P. III., Kimball, B. E., Tolcin, A. C., Guberman, D. E., 2017, Germanium and indium, chap. I of Schulz, K.J, DeYoung, J.H, Jr, Seal, R.R, II, and Bradley, D.C, eds, Critical mineral resources of the United States—Economic and environmental geology and prospects for future supply: U.S. Geological Survey Professional Paper 1802: I1–I27, https://doi.org/10.3133/pp1802I.
Slack, J.F., Shanks III, W.C., Ridley, W.I., Dusel-Bacon, C., DesOrmeau, J.W., Ramezani, J., Fayek, M., 2019. Extreme sulfur isotope fractionation in the Late Devonian Dry Creek volcanogenic massive sulfide deposit, central Alaska. Chem. Geol. 513, 226–238.
Sun, C., Yang, X.Y., Du, G.F., Abdul, Aziz, J.H., 2019. Genesis of the Selinsing gold deposit, Peninsular Malaysia: Constraints from mineralogy, geochemistry and in situ sulfur isotope compositions of sulfides. Ore Geol. Rev. 113, 103111.
Tan, S.C., Zhou, J.X., Luo, K., Xiang, Z.Z., He, X.H., Zhang, Y.H., 2019. The sources of ore-forming elements of the Maoping large-scale Pb-Zn deposit, Yunnan Province: Constrains from in-situ S and Pb isotopes. Acta Petrol. Sin. 35, 3461–3476 (in Chinese with English abstract).
Torró, L., Millán-Nuñez, A.J., Benites, D., González-Jiménez, J.M., Laurent, O., Tavazzani, L., Vallance, J., Chelle-Michou, C., A. Proenza, J., Flores, C., Melgarejo, J. C., Rosas, S., Fontboté, L., 2023. Germanium- and gallium-rich sphalerite in Mississippi Valley-type deposits: the San Vicente district and the Shalipayco deposit, Peru. Miner Deposita. https://doi.org/10.1007/s00126-023-01160-4.
Wei, A.Y., Xue, C.D., Xiang, K., Li, J., Liao, C., Akhter, Q.J., 2015. The ore-forming process of the Maoping Pb-Zn deposit, northeastern Yunnan,China:Constraints from cathodoluminescence(CL) petrography of hydrothermal dolomite. Ore Geol. Rev. 70, 562–577.
Wei, C., Ye, L., Hu, Y.S., Danyushevskiy, L., Li, Z.L., Huang, Z.L., 2019. Distribution and occurrence of Ge and related trace elements in sphalerite from the Lehong carbonate-hosted Zn-Pb deposit, northeastern Yunnan, China: Insights from SEM and LA-ICP-MS studies. Ore Geol. Rev. 115, 103175.
Wei, C., Ye, L., Hu, Y.S., Huang, Z.L., Danyushevskiy, L., Wang, H.Y., 2021. LA-ICP-MS analyses of trace elements in base metal sulfides from carbonate-hosted Zn-Pb deposits, South China: A case study of the Maoping deposit. Ore Geol. Rev. 130, 103945.
Whitehouse, M.J., Kamber, B.S., Fedo, C.M., Lepland, A., 2005. Integrated Pb- and S isotope investigation of sulphide minerals from the early Archaean of southwest Greenland. Chem. Geol. 222, 112–131.
Wood, S.A., Samson, I.M., 2006. The aqueous geochemistry of gallium, germanium, indium and scandium. Ore Geol. Rev. 28, 57–102.
Worden, R.H., Smalley, P.C., Oxtoby, N.H., 1995. Gas souring by the thermo chemical sulfate reduction at 140 °C. AAPG Bull. 79, 854–863.
Wu, T., Huang, Z.L., He, Y.F., Yang, M., Fan, H.F., Chen, W., Ye, L., Hu, Y.S., Xiang, Z.Z., Lai, C.K., 2021. Metal source and ore-forming process of the Maoping carbonate-hosted Pb-Zn deposit in Yunnan, SW China: Evidence from deposit geology and sphalerite Pb-Zn-Cd isotopes. Ore Geol. Rev. 135, 104214.
Wu, Y., Kong, Z.G., Chen, M.H., Zhang, C.Q., Cao, L., Tang, Y.J., Yuan, X., Zhang, P., 2019. Trace elements in sphalerites from the Mississippi Valley-type lead-zinc deposits around the margins of Yangtze Block and its geological implications: A LA-ICPMS study. Acta Petrol. Sin. 35, 3443–3460 (in Chinese with English abstract).
Xiang, Z.Z., Zhou, J.X., Luo, K., 2020. New insights into the multi-layer metallogenesis of carbonated-hosted epigenetic Pb-Zn deposits: A case study of the Maoping Pb-Zn deposit, South China. Ore Geol. Rev. 122, 103538.
Xiao, X., Zhou, T.F., White, N.C., Zhang, L.J., Fan, Y., Wang, F.Y., Chen, X.F., 2018. The formation and trace elements of garnet in the skarn zone from the Xinqiao Cu-S-Fe-Au deposit, Tongling ore district, Anhui Province, Eastern China. Lithos 302–303, 467–479.
Xing, B., Mao, J.W., Xiao, X.N., Liu, H., Jia, F.D., Wang, S.S., Huang, W.Y., Li, H.Y., 2021. Genetic discrimination of the Dingjiashan Pb-Zn deposit, SE China, based on sphalerite chemistry. Ore Geol. Rev. 135, 104212.
Xu, J., Cook, N.J., Ciobanu, C.L., Li, X.F., Kontonikas-Charos, A., Gilbert, S., Lv, Y.H., 2021. Indium distribution in sphalerite from sulfide-oxide-silicate skarn assemblages: a case study of the Dulong Zn-Sn-In deposit, Southwest China. Miner. Deposita 56, 307–324.
Yang, Q., Liu, W. H., Zhang, J., Wang, J., Zhang, X. J., 2019. Formation of Pb-Zn deposits in the Sichuan-Yunnan-Guizhou triangle linked to the Youjiang foreland basin: Evidence from Rb–Sr age and in situ sulfur isotope analysis of the Maoping Pb–Zn deposit in northeastern Yunnan Province, southeast China. Ore Geol. Rev. 107, 780–800.
Ye, L., Cook, N.J., Ciobanu, C.L., Liu, Y.P., Zhang, Q., Liu, T.G., Gao, W., Yang, Y.L., Danyushevskiy, L., 2011. Trace and minor elements in sphalerite from base metal deposits in South China: A LA-ICPMS study. Ore Geol. Rev. 39, 188–217.
Ye, L., Li, Z.L., Hu, Y.S., Huang, Z.L., Zhou, J.X., Fan, H.F., Danyushevskiy, L., 2019. Trace elements in sulfide from the Tianbaoshan Pb-Zn deposit, Sichuan Province, China: A LA-ICPMS study. Acta Petrol. Sin. 32, 3377–3393 (in Chinese with English abstract).
Yu, D.S., Xu, D.R., Zhao, Z.X., Huang, Q.Y., Wang, Z.L., Deng, T., Zou, S.H., 2019. Genesis of the Taolin Pb-Zn deposit in northeastern Hunan Province, South China: constraints from trace elements and oxygen-sulfur-lead isotopes of the hydrothermal minerals. Miner. Deposita 55, 1467–1488.
Yu, D.S., Xu, D.R., Wang, Z.L., Xu, K., Huang, Q.Y., Zou, S.H., Zhao, Z.X., Deng, T., 2021. Trace element geochemistry and O-S-Pb-He-Ar isotopic systematics of the Lishan Pb-Zn-Cu hydrothermal deposit, NE Hunan, South China. Ore Geol. Rev. 133, 104091.
Yuan, B., Zhang, C.Q., Yu, H.J., Yang, Y.M., Zhao, Y.X., Zhu, C.C., Ding, Q.F., Zhou, Y.B., Yang, J.C., Xu, Y., 2018. Element enrichment characteristics: Insights from element geochemistry of sphalerite in Daliangzi Pb-Zn deposit, Sichuan, Southwest China. J. Geochem. Explor. 186, 187–201.
Zhang, H.J., Fan, H.F., Xiao, C.Y., Wen, H.J., Zhu, X.K., Ye, L., Huang, Z.L., Zhou, J.X., 2019. Homogeneous Zn isotopic compositions in the Maozu Zn-Pb ore deposit in Yunnan Province, southwestern China. Ore Geol. Rev. 109, 1–10.
Zhang, R.X., Yang, S.Y., 2016. A mathematical model for determining carbon coating thickness and its application in electron probe microanalysis. Microsc. Microanal. 22, 1374–1380.
Zhou, J.X., Luo, K., Wang, X.C., Wilde, S.A., Wu, T., Huang, Z.L., Cui, Y.L., Zhao, J.X., 2018. Ore genesis of the Fule Pb-Zn deposit and its relationship with the Emeishan Large Igneous Province: Evidence from mineralogy, bulk C-O-S and in situ S-Pb isotopes. Gondwana Res. 54, 161–179.
Zhu, Z.Y., Jiang, S.Y., Ciobanu, C.L., Yang, T., Cook, N.J., 2017. Sulfur isotope fractionation in pyrite during laser ablation: implications for laser ablation multiple collectors inductively coupled plasma mass spectrometry mapping. Chem. Geol. 450, 223–234.